University of Science and Technology of Hanoi

Mean-field study of the equation of states of nuclear matter and tidal deformation of neutron star

Bachelor Thesis

Author:
Nguyen Hoang Dang Khoa

Supervisors:
Prof. Dao Tien Khoa
Dr. Ngo Hai Tan

July 8, 2021

Contents

List of Abbreviations **2**

List of Tables **3**

List of Figures **4**

1 Introduction **6**

2 Hartree-Fock Formalism of Nuclear Matter **9**
2.1 Nucleon-Nucleon Interaction 9
2.2 Equation of States of Nuclear Matter 10
2.3 β-Stable Nuclear Matter 13
2.4 Density dependence of the spin polarization 14

3 Neutron Star Properties **16**
3.1 Mass and Radii 16
3.2 Gravito-electric and Gravito-magnetic Tidal Deformation 17

4 Results and Discussions **20**

5 Conclusions **31**

Bibliography **32**

List of Abbreviations

APR	Akmal, Pandharipande and Ravenhall
BH	Black hole
BHF	Brueckner-Hartree-Fock
CFL	Confident level
DU	Direct Urca
EoS	Equation of States
GE	Gravito-electric
GM	Gravito-magnetic
GR	General Relativity
GRB	Gamma-ray burst
GW	Gravitational wave
HF	Hartree-Fock
HI	Heavy-ion
MMC	Microscopic Monte Carlo
NM	Nuclear Matter
NN	Nucleon-Nucleon
NS	Neutron Star
PSR	Pulsar
TOV	Tolmann-Oppenheimer-Volkoff

List of Tables

2.1 CDM3Yn and BDM3Y1 interaction's parameters; the 00 and 01 terms are inherited from (Tan et al., 2021), while the 10 and 11 parameters are added by fitting with BHF result and K is the incompressibility (2.19) of spin-saturated symmetric NM at saturation density $n_0 \approx 0.17\, fm^{-3}$. 11
2.2 Yukawa strengths of the M3Y-Paris interaction (Tan et al., 2020; Anantaraman et al., 1983). 12

4.1 The symmetry coefficient J, slope parameter L, curvature K_{sym} of the symmetric energy (2.18) and incompressibility K (2.19) of symmetric NM, calculated using 6 different NN interactions. 24

List of Figures

1.1 Neutron star's overall structure. The baryon density decreases (from white to dark gray) as we move outward from the NS center. 7

1.2 Illustration of binary NS merger. (a) The two companion NSs orbit about each others, while gradually losing energy through weak GW and come closer with time. (b) As the two NS get closer, they accelerate and emit stronger GW until (c) colliding, which results in a *kilonova*, characterized by a short *gamma ray burst* (GRB). The product of the merger has yet been decided to be a black hole (BH) or another NS. 8

2.1 Energy per baryon E/A of symmetric NM by the 5 CDM3Yn and BDM3Y1 models compared to BHF result (Vidana and Bombaci, 2002). The diamond and square represent the BHF result for $\Delta_n = -\Delta_p = \pm 1$ and $\Delta_n = \Delta_p = \pm 1$ respectively with Δ_τ being the baryon spin polarization. 10

2.2 Scenarios of the density-dependence of the baryon spin polarization at 3 levels of Δ_0. 15

4.1 Proton fraction x_p of β-stable NM at different baryon density and spin polarization for different density-dependent NN interactions. The lower horizontal lines are the DU threshold (4.2) and the dot at the end of each line corresponds to the highest mass NS's central density of each model. The two rows of figures correspond to two previously defined scenarios, i.e. A and B. 21

4.2 Symmetric energy S of symmetric NM at increasing polarization with 5 CDM3Yn interaction models. The shaded areas are the empirical ranges obtained from the Bayesian study (Xie and Li, 2019) of the NS of radius $R_{1.4}$ at 68% and 90% confident level (CFL) with the GW170817 event (Abbott et al., 2018). The square and triangle are the values suggested by the structure study of Trippa et al. (2008) and Furnstahl (2002). The circles and stars are the ab-initio result of Akmal et al. (1998) (APR) and microscopic Monte Carlo (MMC) calculation by Gandolfi et al. (2010). 22

4.3 Same as Figure 4.2 for the energy per baryon E/A of symmetric NM. 23

4.4 Same as Figure 4.2 for the pressure P as a function of *rest baryon mass density* ρ_b along with empirical pressure given by the "Spectral" EoS from the Bayesian analysis of the GW170817 data (Abbott et al., 2018) with 50% (light gray) and 90% (dark gray) confidence level. The dot at the end of each line corresponds to the central baryon density n_b of maximum NS mass. 25
4.5 The relation between gravitational mass M and the radius R of the NS according to the corresponding model and polarization. The GW170817 constraint for NS with mass $1.4M_\odot$ is shown by the colored contour, where the blue (red) shaded area represents the heavier (lighter) NS (Abbott et al., 2018). The dot in each line indicates the maximum NS mass of the each model. The dark and light orange region indicates the mass of the second PSR J0348+0432 (Antoniadis et al., 2013) and millisecond PSR J0740+6620 (Cromartie et al., 2020) respectively. . . 26
4.6 GE tidal Love number at l^{th} order k_l as function of NS mass computed with 6 density-dependent NN interaction versions at different spin polarizations. The dot at the end of each line represents the maximum gravitational mass M of the NS generated by the corresponding EoS. 27
4.7 Dimensionless GE tidal deformability parameter of 2^{nd} order Λ_2 of different CDM3Yn models with varying Δ. The vertical bar is the empirical tidal deformability constraint $\Lambda_2 \approx 190^{+390}_{-120}$ at $1.4M_\odot$, obtained from the Bayesian analysis of GW170817 data with 90% confidence level (Abbott et al., 2018). 28
4.8 GM tidal Love number at l^{nd} order j_l as function of NS mass computed with CDM3Yn models of *strictly static fluid* at different polarizations. 29
4.9 GM tidal Love number at l^{nd} order j_l as function of NS mass computed with CDM3Yn models of *irrotational fluid* at different polarizations. 30

Chapter 1

Introduction

Neutron stars (NS) are star-like astronomical objects with mass M on the order of solar mass ($M_\odot$), a radius of $\sim 10 - 12\ km$ and an average density n several times greater than that of nucleon ($n_0 \approx 0.17\ fm^{-3}$). They are arguably the densest accessible objects, excluding black holes which we know nothing about inside the event horizon, in the universe (Baym and Pethick, 1975). Due to extremely high density, the matter on NS mainly consists of neutrons that are closely packed together with a small percentage of other particles (p, e^-, ...), similar to a atomic nucleus on macroscopic scale. For this reason, they are also the ideal objects for testing physical theories of dense matter and provide connections between different field of physics, i.e. nuclear physics, elementary particle physics and astrophysics (Lattimer and Prakash, 2004).

During the NS's formation process, protons (p) and electrons (e^-) combined together to form neutrons, i.e.

$$p + e^- \longrightarrow n + \nu_e \tag{1.1}$$

and the star only holds itself against gravity by its own degeneracy pressure and strong force repulsion, which explains why the matter on NS is neutron-dominant and hence the name "neutron stars". After the NS is formed, energy quickly dissipates through neutrino emission, resulting in a relatively cold NS. In this study, we will only concern with the NS after a considerable time from its formation, when the temperature is considered to be $T = 0\ K$.

On a NS, the matter exists as an inhomogenous, low-density *crust* and gradually becomes a more uniform *core* the closer to the NS center as in Figure 1.1. In order to study about the properties of NS matter, the problem have to be approached from the nuclear physics point of view, where we study about *nuclear matter* (NM). For a nuclear system as massive as a NS, we consider one with infinite number of nucleons that are in β-stable state with a small portion of leptons, in which the properties of matter are described using an *equation of states* (EoS), i.e. the relation between different state variables (pressure P, mass-energy density ε, ...) of the system. Ideally, the EoS can be derived from the interactions of quarks under strong force in the framework of quantum chromodynamics. However, due to this having yet to be possible at the moment, the EoS of NM is instead interpreted from a nonrelativistic mean-field study approach with several updated versions of the realistic density-dependent NN interaction models (Tan et al., 2021) using Hartree-Fock (HF) formalism, which will be implemented further in Chapter 2. These models will also be extended to describe the spin polarization phenomena

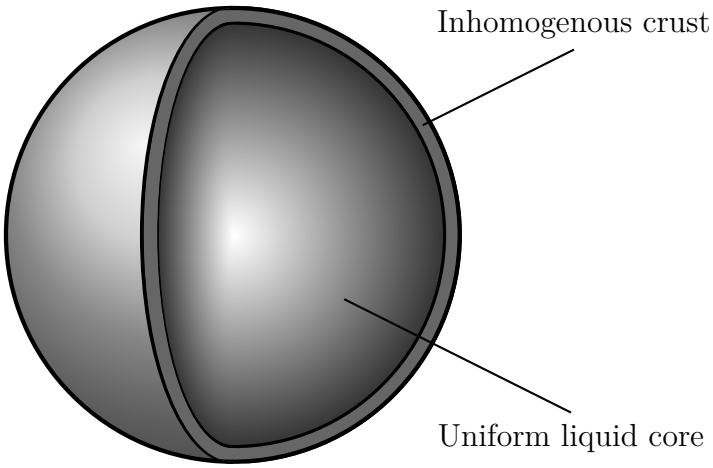

Figure 1.1: Neutron star's overall structure. The baryon density decreases (from white to dark gray) as we move outward from the NS center.

of NM under strong magnetic field such as that in a *magnetar* (a NS that possesses extremely powerful magnetic field).

Following the gravitational wave (GW) signals of the events GW170817 (Abbott et al., 2017) and GW190425 (Abbott et al., 2020) from two binary NS mergers observed by LIGO and Virgo laser interferometer in 17^{th} August 2017 and 25^{th} April 2019 respectively, the tidal deformation of the NS can be further constrained, as well as the mass M and radius R of the NS (Abbott et al., 2018). The NS merger event is illustrated as in Figure 1.2.

Apparently, the EoS of high-density NM plays the most important role in deciding the macroscopic properties of NS. In particular, given the EoS of the crust from the compressible liquid drop model and by using the EoS of the uniform NS core from the result of the HF calculation of cold β-stable NM, the gravitational mass and radius of the star can be decided by the framework of General Relativity (GR) (Tan et al., 2020, 2021), i.e. the Tolman-Oppenheimer-Volkoff (TOV) equation, which will in turn be compared to the observational astrophysical constraints to deduce the most suitable EoS of the constituent NS in this system.

In addition, due to the enormous mass, each NS possesses powerful gravitational field and therefore, they tend to "stretch out" their companion under the tidal effect as in Figure 1.2, while orbiting spirally toward each others and dissipating energy under the form of GW. Particularly, the shape and mass-energy distribution of the NS are tidally deformed from its supposedly spherical shape, resulting in nonzero multipole moments (Hinderer, 2008; Hinderer et al., 2010; Damour and Nagar, 2009). The NS's reaction, i.e. how strongly it deforms when being under a tidal field, is expressed in terms of the *tidal Love numbers* k_l of several orders l, where in this study, we will evaluate the Love number of NS up to the 4^{th} order, i.e. $l = 2, 3, 4$ (Perot and Chamel, 2021). Apparently, the tidal Love number depends heavily on the EoS of matter and this dependence will be further emphasized in Chapter 3. For NS, the central density can be

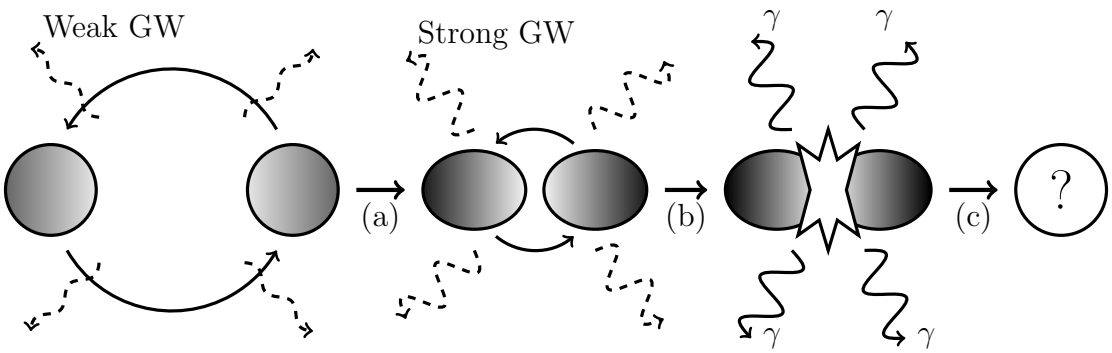

Figure 1.2: Illustration of binary NS merger. (a) The two companion NSs orbit about each others, while gradually losing energy through weak GW and come closer with time. (b) As the two NS get closer, they accelerate and emit stronger GW until (c) colliding, which results in a *kilonova*, characterized by a short *gamma ray burst* (GRB). The product of the merger has yet been decided to be a black hole (BH) or another NS.

up to $6n_0$ and possesses a Love number of order ~ 0.1, while our Earth has that of 0.3. In a recent study, the Love number was calculated for spinning black holes, which showed that even with nearly infinite density, they still posess a small Love number of 0.002 (Le Tiec and Casals, 2021).

Furthermore, under small perturbation of spacetime, the tidal field can also be separated into two components: the *gravito-electric* (GE) and *gravito-magnetic* (GM) terms (Damour and Nagar, 2009) that are analogous to that in eletromagnetic field. As a result, the deformation of the NS, i.e. Love numbers, in the perturbed tidal field can also be categorized into the corresponding GE (k_l) and GM (j_l) components (Perot and Chamel, 2021), whose result will be presented in more details in Chapter 3. To sum up, this study is dedicated to:

- Include the spin polarization effect to the existing CDM3Yn and BDM3Y1 models (Tan et al., 2021),
- Assess the dependence of NS's gravitational mass and radius to different EoS,
- Investigate the sensitivity of GE and GM tidal deformability and Love numbers to NM properties,
- Compare some of the NS's calculated properties to the empirical astrophysical constraints obtained in recent studies (Abbott et al., 2018; Xie and Li, 2019).

Chapter 2

Hartree-Fock Formalism of Nuclear Matter

2.1 Nucleon-Nucleon Interaction

Due to the lack of a exact theory to describe the nucleon-nucleon (NN) interaction, a model need to be imposed and fit with experimental measurement or theoretical calculation results. Plus, for a system as massive as a NS, deducing the EoS using the *ab initio* method, i.e. solving the Schrödinger equation over all particles, is simply impossible, therefore an *effective interaction* must be used (Greiner and Maruhn, 1996). In this section, we only limit ourselves to two-body interaction, thus, the NN potential can be expressed in the form of

$$v = v(\boldsymbol{r}, \boldsymbol{r'}, \boldsymbol{p}, \boldsymbol{p'}, \boldsymbol{\sigma}, \boldsymbol{\sigma'}, \boldsymbol{\tau}, \boldsymbol{\tau'}) \tag{2.1}$$

where the primed and unprimed variables indicate the properties of 2 nucleons respectively, in which $\boldsymbol{r}$ is the particle's position, $\boldsymbol{p}$ is its momentum, $\boldsymbol{\sigma}$ is its intrinsic spin and $\boldsymbol{\tau}$ is its isospin.

The functional form of v in (2.1) cannot freely take any form but is constrained by many invariance requirements (Greiner and Maruhn, 1996), namely the translational, Galilei, rotational, isospin, parity and time reversal invariance. Having such considerations, developing further the M3Y-Paris interaction, which was used by the HF study of NM (Loan et al., 2011; Tan et al., 2016, 2020, 2021) and the folding model study of NN scattering (Khoa et al., 1997; Khoa and Satchler, 2000),

$$v = v_{00}(r) + v_{10}(r)\boldsymbol{\sigma}\cdot\boldsymbol{\sigma'} + v_{01}(r)\boldsymbol{\tau}\cdot\boldsymbol{\tau'} + v_{11}(r)(\boldsymbol{\sigma}\cdot\boldsymbol{\sigma'})(\boldsymbol{\tau}\cdot\boldsymbol{\tau'}) \tag{2.2}$$

by adding a density-dependent form factor $F_{\sigma\tau}(n)$ to each term gives the CDM3Yn and BDM3Y1 interaction model

$$\begin{aligned} v(n,r) = {} & F_{00}(n)v_{00}(r) + F_{10}(n)v_{10}(r)\boldsymbol{\sigma}\cdot\boldsymbol{\sigma'} \\ & + F_{01}(n)v_{01}(r)\boldsymbol{\tau}\cdot\boldsymbol{\tau'} + F_{11}(n)v_{11}(r)(\boldsymbol{\sigma}\cdot\boldsymbol{\sigma'})(\boldsymbol{\tau}\cdot\boldsymbol{\tau'}) \end{aligned} \tag{2.3}$$

where each radial term is the superposition of 3 Yukawa potentials

$$v_{\sigma\tau}(r) = \sum_{k=1}^{3} Y_{\sigma\tau}(k)\frac{\exp(-\mu_k r)}{\mu_k r} \tag{2.4}$$

and the form factor $F_{\sigma\tau}(n)$ shared the functional form (Khoa et al., 1997; Tan et al., 2020, 2021; Thân, 2010)

$$F_{\sigma\tau}(n) = C_{\sigma\tau}[1 + \alpha_{\sigma\tau}\exp(-\beta_{\sigma\tau}n) + \gamma_{\sigma\tau}n] \tag{2.5}$$

with parameters given in Table 2.1. The parameters of F_{00} were adjusted to give the corresponding values of incompressibility K of symmetric NM at saturation density n_0 and the binding energy $E_0 \approx 15.8\ MeV$, while the 10 term is modified from (Thân, 2010) to reproduce $E_{sym}(n_0) \approx 30\ MeV$, $L \approx 50\ MeV$ and to be in agreement with the ab-initio results (Akmal et al., 1998; Gandolfi et al., 2010) at higher density (Tan et al., 2021). On the other hand, the spin-dependent terms, 10 and 11, are hereby included in the 5 models by fine tuning the parameters to yield the same result as the Brueckner-Hartree-Fock (BHF) study of spin polarized NM (Vidana and Bombaci, 2002) as in Figure 2.1.

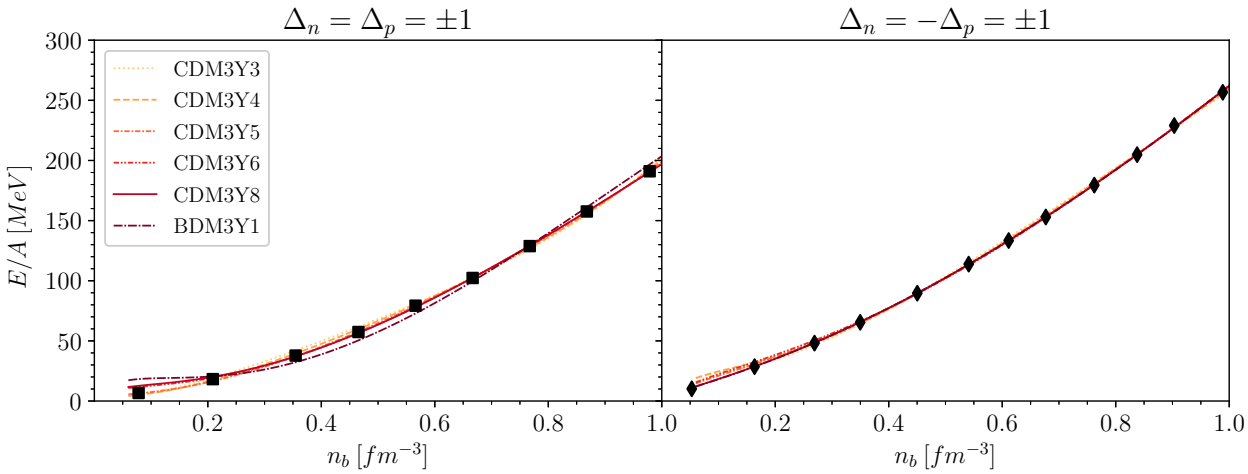

Figure 2.1: Energy per baryon E/A of symmetric NM by the 5 CDM3Yn and BDM3Y1 models compared to BHF result (Vidana and Bombaci, 2002). The diamond and square represent the BHF result for $\Delta_n = -\Delta_p = \pm 1$ and $\Delta_n = \Delta_p = \pm 1$ respectively with Δ_τ being the baryon spin polarization.

2.2 Equation of States of Nuclear Matter

In HF formalism, the total HF energy of the system can be expressed as

$$\begin{aligned} E_{HF} = \sum_{\sigma\tau}\sum_{\boldsymbol{k}}^{k_F^{\sigma\tau}} \frac{\hbar^2 k^2}{2m_\tau} + \frac{1}{2}\sum_{\boldsymbol{k}\sigma\tau}\sum_{\boldsymbol{k'}\sigma'\tau'} \Big[\Big\langle \boldsymbol{k}\sigma\tau, \boldsymbol{k'}\sigma'\tau' \Big| v^D \Big| \boldsymbol{k}\sigma\tau, \boldsymbol{k'}\sigma'\tau' \Big\rangle \\ + \Big\langle \boldsymbol{k}\sigma\tau, \boldsymbol{k'}\sigma'\tau' \Big| v^{EX} \Big| \boldsymbol{k'}\sigma\tau, \boldsymbol{k}\sigma'\tau' \Big\rangle \Big] \end{aligned} \tag{2.6}$$

where the single-particle wave function is plane wave

$$|\boldsymbol{k}\sigma\tau\rangle = \frac{e^{i\boldsymbol{k}\cdot\boldsymbol{r}}}{\sqrt{\Omega}}\chi_\sigma\chi_\tau \tag{2.7}$$

Table 2.1: CDM3Yn and BDM3Y1 interaction's parameters; the 00 and 01 terms are inherited from (Tan et al., 2021), while the 10 and 11 parameters are added by fitting with BHF result and K is the incompressibility (2.19) of spin-saturated symmetric NM at saturation density $n_0 \approx 0.17\, fm^{-3}$.

Interaction	$\sigma\tau$	$C_{\sigma\tau}$	$\alpha_{\sigma\tau}$	$\beta_{\sigma\tau}$ (fm^3)	$\gamma_{\sigma\tau}$ (fm^3)	K (MeV)
CDM3Y3	00	0.2985	3.4528	2.6388	−1.5	217
	01	0.2343	5.3336	6.4738	4.3172	
	10	0.3890	3.5635	−2.6717	20.3624	
	11	0.8802	4.0433	12.3262	0.3662	
CDM3Y4	00	0.3052	3.2998	2.3180	−2.0	228
	01	0.2129	6.3581	7.0584	5.6091	
	10	0.2593	6.0016	−2.3377	18.8725	
	11	0.8329	3.5941	9.2012	0.2690	
CDM3Y5	00	0.2728	3.7367	1.8294	−3.0	241
	01	0.2204	6.6146	7.9910	6.0040	
	10	0.4106	5.6265	−1.6698	−1.9866	
	11	0.6815	2.5833	5.1700	0.2578	
CDM3Y6	00	0.2658	3.8033	1.4099	−4.0	252
	01	0.2313	6.6865	8.6775	6.0182	
	10	0.5186	9.9402	1.6698	2.9799	
	11	0.6058	3.1947	4.4512	0.0822	
CDM3Y8	00	0.2658	3.8033	1.4099	−4.3	257
	01	0.2643	6.3836	9.8950	5.4249	
	10	0.5997	9.1900	0.7514	−4.7181	
	11	0.3786	3.9435	2.7012	0.3512	
BDM3Y1	00	1.2521	0.0	0.0	−1.7452	270
	01	0.2528	7.6996	11.0386	6.3568	
	10	−1.3226	−8.2559	0.0	17.2307	
	11	0.1654	9.7394	1.6714	−1.4893	

with Ω being the spatial volume of the system, $k_F^{\sigma\tau} = (6\pi^2 n_{\sigma\tau})^{1/3}$ is the Fermi momentum corresponding to spin σ and isospin τ, $v^{D(EX)}$ is the direct (exchange) part of the interaction determined from the singlet and triplet-even (odd) of the central NN force. Adopting the same functional form of (2.3), the direct and exchange interaction is written as

$$\begin{aligned} v^{D(EX)}(n_b, r) = {} & F_{00}(n_b) v_{00}^{D(EX)}(r) + F_{10}(n_b) v_{10}^{D(EX)}(r) \boldsymbol{\sigma} \cdot \boldsymbol{\sigma'} \\ & + F_{01}(n_b) v_{01}^{D(EX)}(r) \boldsymbol{\tau} \cdot \boldsymbol{\tau'} + F_{11}(n_b) v_{11}^{D(EX)}(r) (\boldsymbol{\sigma} \cdot \boldsymbol{\sigma'})(\boldsymbol{\tau} \cdot \boldsymbol{\tau'}) \end{aligned} \tag{2.8}$$

and

$$v_{\sigma\tau}^{D(EX)}(r) = \sum_{k=1}^{3} Y_{\sigma\tau}^{D(EX)}(k) \frac{\exp(-\mu_k r)}{\mu_k r} \tag{2.9}$$

with the Yukawa strengths given in Table 2.2 and the density-dependent form factor parameters are in Table 2.1. Note that in (2.8), n_b denotes the *baryon density*, this will be used in order to distinguish with the lepton density in the later section.

Table 2.2: Yukawa strengths of the M3Y-Paris interaction (Tan et al., 2020; Anantaraman et al., 1983).

k	μ_k (fm^{-1})	Y_{00}^D (MeV)	Y_{10}^D (MeV)	Y_{01}^D (MeV)	Y_{11}^D (MeV)
1	4.0	11061.625	938.875	313.625	−969.125
2	2.5	−2537.5	−36.0	223.5	450.0
3	0.7072	0.0	0.0	0.0	3.4877
k	μ_k (fm^{-1})	Y_{00}^{EX} (MeV)	Y_{10}^{EX} (MeV)	Y_{01}^{EX} (MeV)	Y_{11}^{EX} (MeV)
1	4.0	−1524.25	−3492.75	−4118.0	−2210.0
2	2.5	−518.75	795.25	1054.75	568.75
3	0.7072	−7.8474	2.6157	2.6157	−0.8719

Multiply (2.6) with Ω^{-1}, the energy density of the NM is separated into the kinetic term ε_{kin} and the potential terms $\varepsilon_{\sigma\tau}$, i.e.

$$\varepsilon_{HF} = \frac{E_{HF}}{\Omega} = \varepsilon_{kin} + F_{00}(n_b)\varepsilon_{00} + F_{01}(n_b)\varepsilon_{01} + F_{10}(n_b)\varepsilon_{10} + F_{11}(n_b)\varepsilon_{11} \tag{2.10}$$

The final expressions of each terms of the energy density are

$$\varepsilon_{kin} = \frac{3}{10}\sum_{\sigma\tau}\frac{\hbar^2(k_F^{\sigma\tau})^2}{m_\tau}n_{\sigma\tau} \tag{2.11}$$

$$\varepsilon_{00} = \frac{1}{2}\left[n_b^2 J_{00}^D + \int A_{00}^2 v_{00}^{EX}(r)\, d^3r\right] \tag{2.12}$$

$$\varepsilon_{10} = \frac{1}{2}\left[n_b^2 J_{10}^D\left(\Delta_n\frac{1+\delta}{2} + \Delta_p\frac{1-\delta}{2}\right)^2 + \int A_{10}^2 v_{10}^{EX}(r)\, d^3r\right] \tag{2.13}$$

$$\varepsilon_{01} = \frac{1}{2}\left[n_b^2 J_{01}^D\delta^2 + \int A_{01}^2 v_{01}^{EX}(r)\, d^3r\right] \tag{2.14}$$

$$\varepsilon_{11} = \frac{1}{2}\left[n_b^2 J_{11}^D\left(\Delta_n\frac{1+\delta}{2} - \Delta_p\frac{1-\delta}{2}\right)^2 + \int A_{11}^2 v_{11}^{EX}(r)\, d^3r\right] \tag{2.15}$$

where $\Delta_\tau = (n_{\uparrow\tau} - n_{\downarrow\tau})/n_\tau$ is the polarization of nucleon, $\delta = (n_n - n_p)/n_b$ is the asymmetry of NM, $J_{\sigma\tau}^D = \int v_{\sigma\tau}^D(r)\, d^3r$ is the volume integral of the direct interaction and

$$\begin{aligned}
A_{00} &= n_{\uparrow n}\hat{j}_1(k_F^{\uparrow n}r) + n_{\downarrow n}\hat{j}_1(k_F^{\downarrow n}r) + n_{\uparrow p}\hat{j}_1(k_F^{\uparrow p}r) + n_{\downarrow p}\hat{j}_1(k_F^{\downarrow p}r)\\
A_{10} &= n_{\uparrow n}\hat{j}_1(k_F^{\uparrow n}r) - n_{\downarrow n}\hat{j}_1(k_F^{\downarrow n}r) + n_{\uparrow p}\hat{j}_1(k_F^{\uparrow p}r) - n_{\downarrow p}\hat{j}_1(k_F^{\downarrow p}r)\\
A_{01} &= n_{\uparrow n}\hat{j}_1(k_F^{\uparrow n}r) + n_{\downarrow n}\hat{j}_1(k_F^{\downarrow n}r) - n_{\uparrow p}\hat{j}_1(k_F^{\uparrow p}r) - n_{\downarrow p}\hat{j}_1(k_F^{\downarrow p}r)\\
A_{11} &= n_{\uparrow n}\hat{j}_1(k_F^{\uparrow n}r) - n_{\downarrow n}\hat{j}_1(k_F^{\downarrow n}r) - n_{\uparrow p}\hat{j}_1(k_F^{\uparrow p}r) + n_{\downarrow p}\hat{j}_1(k_F^{\downarrow p}r)
\end{aligned} \tag{2.16}$$

with $\hat{j}_1(x) = 3j_1(x)/x$ and $j_1(x)$ being the 1st order spherical Bessel function.

In the parabolic approximation (Khoa et al., 1996), the energy density per nucleon E/A can also be expanded in terms of the asymmetry δ as

$$\frac{E}{A}(n_b, \delta, \Delta_n, \Delta_p) = \frac{\varepsilon_{HF}}{n_b} = \frac{E}{A}(n_b, \delta = 0, \Delta_n, \Delta_p) + S(n_b, \Delta_n, \Delta_p)\delta^2 + \mathcal{O}(\delta^4) \tag{2.17}$$

with S being the *nuclear symmetry energy*. The symmetry coefficient J, slope parameter L and curvature K_{sym} are taken by expanding the symmetry energy at saturation density n_0, i.e. (Tan et al., 2020; Li et al., 2008; Horowitz et al., 2014; Lattimer, 2014)

$$S(n_b, \Delta_n, \Delta_p) = J(\Delta_n, \Delta_p) + \frac{L(\Delta_n, \Delta_p)}{3}\left(\frac{n_b - n_0}{n_0}\right) + \frac{K_{sym}(\Delta_n, \Delta_p)}{18}\left(\frac{n_b - n_0}{n_0}\right)^2 + \dots \tag{2.18}$$

along with the nuclear incompressibility at saturation density

$$K(\Delta_n, \Delta_p) = 9\left.\frac{\partial P(n_b, \delta = 0, \Delta_n, \Delta_p)}{\partial n_b}\right|_{n_b \to n_0} \tag{2.19}$$

These are the quantity that will be used in order to compared with the empirical values in Chapter 4.

2.3 β-Stable Nuclear Matter

After the HF calculation, we were able to obtain a numerical HF energy density ε_{HF}. However, it is in fact impossible for a NS to exist while consisting of purely nucleon. In order to compensate for this issue, leptons (e^- and μ^-) have to be introduced to the matter constituents and the $npe\mu$ matter has to satisfy the *β-stable* condition (Glendenning, 2012), i.e.

- Charge balance
$$n_p = n_e + n_\mu \tag{2.20}$$
- Chemical potential balance
$$\mu_n - \mu_p = \mu_e = \mu_\mu \tag{2.21}$$
where $\mu_i = \frac{\partial \varepsilon}{\partial n_i}$ $(i = n, p, e, \mu)$ is the chemical potential of the i particle.

The total energy density of the $npe\mu$ matter is thus

$$\varepsilon = \varepsilon_{HF} + n_n m_n c^2 + n_p m_p c^2 + \varepsilon_e + \varepsilon_\mu \tag{2.22}$$

which leads to the nucleon chemical potential of the form

$$\mu_\tau(n_n, n_p, \Delta_n, \Delta_p) = \frac{\partial \varepsilon}{\partial n_\tau} = \frac{\partial \varepsilon_{HF}}{\partial n_\tau} + m_\tau c^2 \tag{2.23}$$

Let $\hat{\mu} = \mu_n - \mu_p$ be the leptons' chemical potential, (2.20) is equivalent to[1]

$$3\pi^2(\hbar c)^3 n_p - \hat{\mu}^3 - \left[\hat{\mu}^2 - (m_\mu c^2)^2\right]^{3/2}\theta(\hat{\mu} - m_\mu c^2) = 0 \tag{2.24}$$

[1] $\theta(x)$ is the Heaviside function, i.e. it returns 1 for $x \geq 0$ and 0 otherwise.

from which the proton fraction $x_p = n_p/n_b$ can be obtained as shown in Figure 4.1, note that only beyond the muon threshold density $\mu_e > m_\mu c^2 \approx 105.6\, MeV$ do muons appear in the system. Furthermore, under strong magnetic field like that of a magnetar, we can approximate $\Delta_n \approx -\Delta_p \approx \Delta$ and reduce the EoS to depend on just the baryon polarization Δ alone, and the more baryon polarized, the stronger the magnetic field of the NS.

For a fixed value of Δ, we are able to obtain a density function of the form $n_n(n_b, \Delta)$ and $n_p(n_b, \Delta)$, which in turn gives the lepton chemical potential $\hat{\mu}(n_b, \Delta) = \hat{\mu}(n_n, n_p)$ On the other hand, the leptons' densities are then (Loan et al., 2011)

$$n_e(n_b, \Delta) = \frac{\hat{\mu}^3(n_b, \Delta)}{3\pi^2(\hbar c)^3} \quad \text{and} \quad n_\mu(n_b, \Delta) = \frac{\left[\hat{\mu}^2(n_b, \Delta) - (m_\mu c^2)^2\right]^{3/2}}{3\pi^2(\hbar c)^3}\theta(\hat{\mu}(n_b, \Delta) - m_\mu c^2) \quad (2.25)$$

Consider the e^- and μ^- to be systems of relativistic Fermi gas, then their respective energy densities and pressure contributions are ($l = e, \mu$) (Moustakidis and Panos, 2009)

$$\varepsilon_l(n_b, \Delta) = \frac{2}{(2\pi)^3}\int_0^{[3\pi^2 n_l(n_b,\Delta)]^{1/3}} \sqrt{\hbar^2c^2k^2 + m_l^2c^4}\, d^3\mathbf{k} \quad (2.26)$$

and

$$P_l(n_b, \Delta) = \frac{1}{3}\frac{2}{(2\pi)^3}\int_0^{[3\pi^2 n_l(n_b,\Delta)]^{1/3}} \frac{\hbar^2c^2k^2}{\sqrt{\hbar^2c^2k^2 + m_l^2c^4}}\, d^3\mathbf{k} \quad (2.27)$$

Plus, from the HF formalism with NM, the baryon pressure is given by

$$P_b = n_b^2\frac{\partial(\varepsilon_{HF}/n_b)}{\partial n_b} \quad (2.28)$$

Finally, we obtain the total energy density-dependence on baryon density as

$$\varepsilon(n_b, \Delta) = \varepsilon_{HF}(n_b, \Delta) + n_n(n_b, \Delta)m_nc^2 + n_p(n_b, \Delta)m_pc^2 + \varepsilon_e(n_b, \Delta) + \varepsilon_\mu(n_b, \Delta) \quad (2.29)$$

and the total pressure of NS matter

$$P(n_b, \Delta) = P_b(n_b, \Delta) + P_e(n_b, \Delta) + P_\mu(n_b, \Delta) \quad (2.30)$$

In addition, the EoS of the NS's crust (low baryon density region) is adopted from the Compress Liquid Drop Model calculation (Douchin et al., 2000; Douchin and Haensel, 2001). The complete EoS of cold β-stable NS matter is later discussed in Chapter 4.

2.4 Density dependence of the spin polarization

In the above calculation, the baryon spin polarization Δ was taken to be independent of the baryon density n_b; however, due to the complexity of the magnetic field distribution inside the NS (Fujisawa and Kisaka, 2014), this does not fully reflect the reality. Particularly, in the inner core of the NS, baryons are heavily compressed at extremely high density by gravity,

which leads to the full degeneracy, i.e. all possible quantum states are occupied, of baryons in this region and there is no room for baryon to change its spin orientation. Along with the magnetic field, the spin polarization of baryon is expected to gradually weaken to $\Delta \approx 0$ the nearer to the NS center, in other words, at higher density (Fujisawa and Kisaka, 2014; Tan et al., 2020). Although it's beyond the scope of the current study to accurately calculate the density-dependence of $\Delta(n_b)$, we will explore such effect by investigating different scenarios proposed by Tan et al. (2020) based on the magnetic field distribution of magnetar obtained by Fujisawa and Kisaka (2014), i.e.

(A) The magnetic field is strongly localized in the surface region of the NS, near the crust-core transition, and falls to $B \approx 0$ at $n_b \approx 0.18\ fm^{-3}$,

(B) The magnetic field distribution is broader and decreases gradually to zero at a denser region, which cover both the crust and the outer core, of $n_b \approx 0.35\ fm^{-3}$.

Each scenario was considered with $\Delta_0 = \Delta(n_b \approx 0)$ at the value of partial polarization $\Delta_0 = 0.6$, 0.8 and total polarization $\Delta_0 = 1.0$ as shown in Figure 2.2

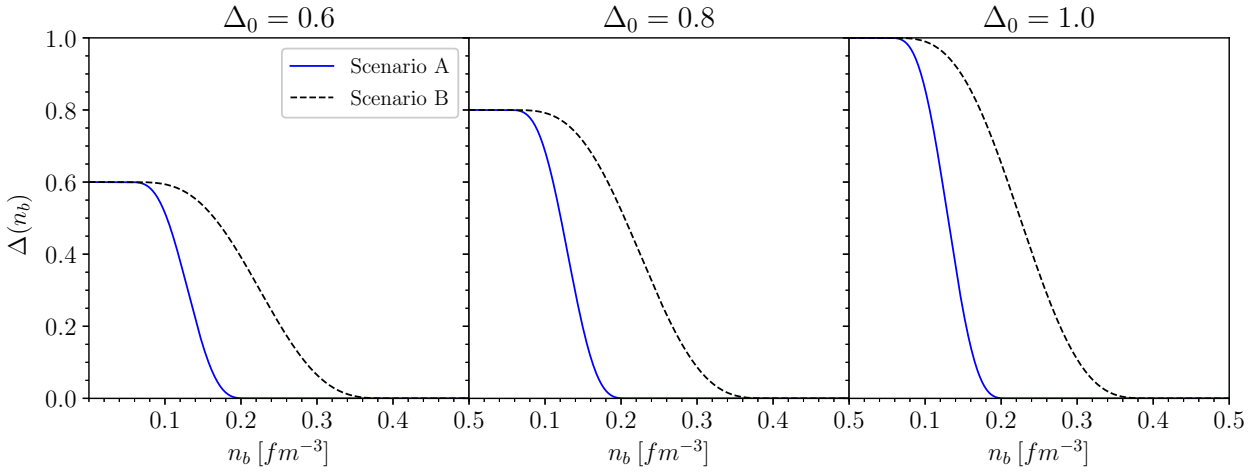

Figure 2.2: Scenarios of the density-dependence of the baryon spin polarization at 3 levels of Δ_0.

Chapter 3

Neutron Star Properties

3.1 Mass and Radii

Suppose the NS to be static and spherically symmetric, the metric elements are then (Glendenning, 2012)

$$\mathrm{d}s^2 = g_{\mu\nu}\mathrm{d}x^\mu \mathrm{d}x^\nu = e^{2\nu(r)}c^2\mathrm{d}t^2 - e^{2\lambda(r)}\mathrm{d}r^2 - r^2\mathrm{d}\theta^2 - r^2\sin^2\theta\mathrm{d}\phi^2 \tag{3.1}$$

Consider the NS matter to be perfect fluid, the energy-momentum tensor of its has the from of

$$T^{\mu\nu} = -Pg^{\mu\nu} + (P+\varepsilon)u^\mu u^\nu \tag{3.2}$$

where $u^\mu = dx^\mu/d\tau$ is the local fluid 4-velocity. Solving the Einstein's field equation

$$G^{\mu\nu} = -\frac{8\pi G}{c^4}T^{\mu\nu} \tag{3.3}$$

gives the Tolman-Oppenheimer-Volkoff (TOV) equation (Glendenning, 2012)

$$\frac{\mathrm{d}P}{\mathrm{d}r} = -\frac{G\varepsilon m}{c^2r^2}\left(1+\frac{P}{\varepsilon}\right)\left(1+\frac{4\pi Pr^3}{mc^2}\right)\left(1-\frac{2Gm}{c^2r}\right)^{-1} \tag{3.4}$$

$$\frac{\mathrm{d}m}{\mathrm{d}r} = \frac{4\pi r^2\varepsilon}{c^2} \tag{3.5}$$

where ε and P are the EoS obtained from the CDM3Yn and BDM3Y1 interactions from the HF calculation previously evaluated. Additional boundary conditions are

$$P(0) = P_c; \qquad P(R) = 0; \qquad m(0) = 0; \qquad m(R) = M$$

By solving the TOV equation (3.4) with the aid of an EoS, one is able to obtain a density (or mass or pressure) profile of the NS matter as a function of distance to the stellar center, and with each value of the central pressure P_c, an unique NS of mass M and radius R is generated. Thus, by varying the center pressure P_c, a relation between M and R of the NS corresponding with each EoS can be found.

3.2 Gravito-electric and Gravito-magnetic Tidal Deformation

In close orbit with another compact companion in a binary system, the NS is tidally deformed by strong gravitational interaction. Analogous to the classical theory of electromagnetism, the tidal field experienced by it can be decomposed into 2 types: the *gravito-electric* and *gravito-magnetic* components with respective *relativistic tidal moment* (Damour and Nagar, 2009)

$$\mathcal{E}_L = \partial_{L-1} E_{a_l} \qquad \text{and} \qquad \mathcal{M}_L = c^2 \partial_{L-1} B_{a_l} \tag{3.6}$$

where E_{a_l} and B_{a_l} are the a_l component of the externally generated local GE and GM field, L represents the multi-index $(a_1, a_2, \ldots, a_l)$ and l being the order of the moment. As a result, the deformation of NS is parameterized by the GE and GM *tidal deformabilities* λ_l and σ_l, i.e. in leading order (Damour and Nagar, 2009)

$$\mathcal{Q}_L = \lambda_l \mathcal{E}_L, \tag{3.7}$$
$$\mathcal{S}_L = \sigma_l \mathcal{M}_L \tag{3.8}$$

with $\mathcal{Q}_L$ being the induced mass multipole moment, i.e. the deviation of the mass distribution from spherically symmetry at order l, while $\mathcal{S}_L$ is the current multipole moment in adiabatic approximation (Damour and Nagar, 2009; Perot and Chamel, 2021). From the deformabilities, the dimensionless GE and GM *tidal Love numbers* are defined as (Perot and Chamel, 2021)

$$k_l = \frac{1}{2}(2l-1)!! \frac{G\lambda_l}{R^{2l+1}} \quad \text{and} \quad j_l = 4(2l-1)!! \frac{G\sigma_l}{R^{2l+1}} \tag{3.9}$$

These parameters are directly related to the GE and GM *tidal deformability parameters* as

$$\Lambda_l = \frac{2}{(2l-1)!!} k_l \left(\frac{c^2 R}{GM}\right)^{2l+1} \tag{3.10}$$
$$\Sigma_l = \frac{1}{4(2l-1)!!} j_l \left(\frac{c^2 R}{GM}\right)^{2l+1} \tag{3.11}$$

which can be potentially extracted from the signal of GW. In order to properly calculate these parameters, let $H_l(r)$ and $\tilde{H}_l(r)$ characterize small perturbations of the static metric. These functions have to satisfy (Perot and Chamel, 2021; Damour and Nagar, 2009)

$$\begin{aligned} &H_l''(r) + H_l'(r)\left[1 - \frac{2Gm(r)}{c^2 r}\right]^{-1} \left\{\frac{2}{r} - \frac{2Gm(r)}{c^2 r^2} - \frac{4\pi G}{c^4} r[\varepsilon(r) - P(r)]\right\} \\ &+ H_l(r)\left[1 - \frac{2Gm(r)}{c^2 r}\right]^{-1} \left\{\frac{4\pi G}{c^4}\left[5\varepsilon(r) + 9P(r) + c^2 \frac{\mathrm{d}\varepsilon}{\mathrm{d}P}[\varepsilon(r) + P(r)]\right]\right. \\ &\left. - \frac{l(l+1)}{r^2} - 4\left[1 - \frac{2Gm(r)}{c^2 r}\right]^{-1}\left[\frac{Gm(r)}{c^2 r^2} + \frac{4\pi G}{c^4} r P(r)\right]^2\right\} = 0 \end{aligned} \tag{3.12}$$

for GE perturbations and

$$\tilde{H}_l''(r) - \tilde{H}_l'(r)\left[1-\frac{2Gm(r)}{c^2r}\right]^{-1}\frac{4\pi G}{c^4}r\left[P(r)+\varepsilon(r)\right]$$
$$-\tilde{H}_l(r)\left[1-\frac{2Gm(r)}{c^2r}\right]^{-1}\left\{\frac{l(l+1)}{r^2}-\frac{4Gm(r)}{c^2r^3}+\theta\frac{8\pi G}{c^4}\left[P(r)+\varepsilon(r)\right]\right\}=0 \quad (3.13)$$

for GM perturbations; the value of $\theta = 1$ is for static fluid while irrotational fluid adopts the value $\theta = -1$. These two equations are integrated along with the TOV equation (3.4). In addition, we have the compactness parameters $C = GM/(Rc^2)$ and define

$$y_l = \frac{RH_l'(R)}{H_l(R)} \quad \text{and} \quad \tilde{y}_l = \frac{R\tilde{H}_l'(R)}{\tilde{H}_l(R)}. \quad (3.14)$$

The explicit expressions of the first few orders of the GE and GM Love numbers are

$$k_2 = \frac{8}{5}C^5(1-2C)^2\left[2(y_2-1)C-y_2+2\right]\Big\{2C\Big[4(y_2+1)C^4+2(3y_2-2)C^3$$
$$-2(11y_2-13)C^2+3(5y_2-8)C-3(y_2-2)\Big]$$
$$+3(1-2C)^2\left[2(y_2-1)C-y_2+2\right]\log(1-2C)\Big\}^{-1}, \quad (3.15)$$

$$k_3 = \frac{8}{7}C^7(1-2C)^2\Big[2(y_3-1)C^2-3(y_3-2)C+y_3-3\Big]$$
$$\times\Big\{2C\Big[4(y_3+1)C^5+2(9y_3-2)C^4-20(7y_3-9)C^3+5(37y_3-72)C^2-45(2y_3-5)C$$
$$+15(y_3-3)\Big]+15(1-2C)^2\Big[2(y_3-1)C^2-3(y_3-2)C+y_3-3\Big]\log(1-2C)\Big\}^{-1}, \quad (3.16)$$

$$k_4 = \frac{32}{147}C^9(1-2C)^2\Big[12(y_4-1)C^3-34(y_4-2)C^2+28(y_4-3)C-7(y_4-4)\Big]$$
$$\times\Big\{2C\Big[8(y_4+1)C^6+4(17y_4-2)C^5-12(83y_4-107)C^4+40(55y_4-116)C^3$$
$$-10(191y_4-536)C^2+105(7y_4-24)C-105(y_4-4)\Big]+15(1-2C)^2\Big[12(y_4-1)C^3$$
$$-34(y_4-2)C^2+28(y_4-3)C-7(y_4-4)\Big]\log(1-2C)\Big\}^{-1}, \quad (3.17)$$

$$j_2 = \frac{24}{5}C^5\left[2(\tilde{y}_2-2)C-\tilde{y}_2+3\right]\Big\{2C\Big[2(\tilde{y}_2+1)C^3+2\tilde{y}_2C^2+3(\tilde{y}_2-1)C-3(\tilde{y}_2-3)\Big]$$
$$+3\left[2(\tilde{y}_2-2)C-\tilde{y}_2+3\right]\log(1-2C)\Big\}^{-1}, \quad (3.18)$$

$$j_3 = \frac{64}{21}C^7\Big[8(\tilde{y}_3-2)C^2-10(\tilde{y}_3-3)C+3(\tilde{y}_3-4)\Big]$$
$$\times\Big\{2C\Big[4(\tilde{y}_3+1)C^4+10\tilde{y}_3C^3+30(\tilde{y}_3-1)C^2-15(7\tilde{y}_3-18)C+45(\tilde{y}_3-4)\Big]$$
$$+15\Big[8(\tilde{y}_3-2)C^2-10(\tilde{y}_3-3)C+3(\tilde{y}_3-4)\Big]\log(1-2C)\Big\}^{-1}, \quad (3.19)$$

$$j_4 = \frac{80}{147}C^9\Big[40(\tilde{y}_4-2)C^3-90(\tilde{y}_4-3)C^2+63(\tilde{y}_4-4)C-14(\tilde{y}_4-5)\Big]$$
$$\times\Big\{2C\Big[4(\tilde{y}_4+1)C^5+18\tilde{y}_4C^4+90(\tilde{y}_4-1)C^3-5(137\tilde{y}_4-334)C^2$$
$$+105(7\tilde{y}_4-26)C-210(\tilde{y}_4-5)\Big]+15\Big[40(\tilde{y}_4-2)C^3-90(\tilde{y}_4-3)C^2$$

$$+63(\tilde{y}_4 - 4)C - 14(\tilde{y}_4 - 5)\Big] \log(1 - 2C)\Big\}^{-1}$$

as derived by Damour and Nagar (2009) and Perot and Chamel (2021).

Chapter 4

Results and Discussions

Under the condition of β-stable, the proton's contribution $x_p = n_p/n_b$ to the baryon density of of neutrino-free NS matter is given by Figure 4.1, computed with 5 different versions of the density-dependent NN interaction. It can be seen that in all cases, the higher the density, the more protons there are in the baryon composition. Furthermore, with the newly introduced parameterization of spin-dependent terms (10 and 11) in all 6 interactions, generally the protons are more abundant at higher polarization, which can be seen with the height of each "bump" in Figure 4.1 at low density, while the highes mass possible NS for each configuration tends to decrease with increasing incompressibility K, i.e. different model. The density-dependent proton fraction x_p is also an essential input for determining the cooling rate of the NS, in which the dominant direct Urca (DU) process of NS cooling by ν emission (Lattimer and Prakash, 2004), i.e.

$$n \longrightarrow p + e^- + \bar{\nu}_e \quad \text{and} \quad p \longrightarrow n + e^+ + \nu_e, \tag{4.1}$$

can only take place if the proton fraction exceeds the threshold (Loan et al., 2011)

$$x_{DU} = \frac{1}{1 + \left[1 + \left(\frac{n_e}{n_e + n_\mu}\right)^{1/3}\right]^3} \tag{4.2}$$

Note that the thresholds x_{DU} determined in these calculations remain fairly unchanged in the whole range of baryon density, as well as when the polarization varies or at different models, which can be explained by the absence of interaction between leptons and baryons in the current study. The threshold also ranges from $\approx 11\%$ at low density, due to the absence of muon, to $\approx 15\%$ as n_b increases, which is consistent with the range deduced from the study of Lattimer et al. (1991). The proton fraction x_p in this case increases significantly as the value of Δ_0 rises to ≈ 1, however, due to the localization of magnetic field in the surface, all models in the two scenarios commonly surpass the DU threshold at a high density of $\lesssim 5n_0$. Beside, the electron fraction infered by this result is around $\gtrsim 10\%$, which is however much lower than the observed quantity $\approx 27\%$ from the blue kilonova ejecta following the GW170817 event (Abbott et al., 2017; Evans et al., 2017) and can very possibly come from a magnetar as suggested by Metzger et al. (2018).

The nuclear symmetry energy is well constrained at low baryon density by the study of heavy-ion (HI) collisions (Tsang et al., 2011; Ono et al., 2003), the structure study of the giant

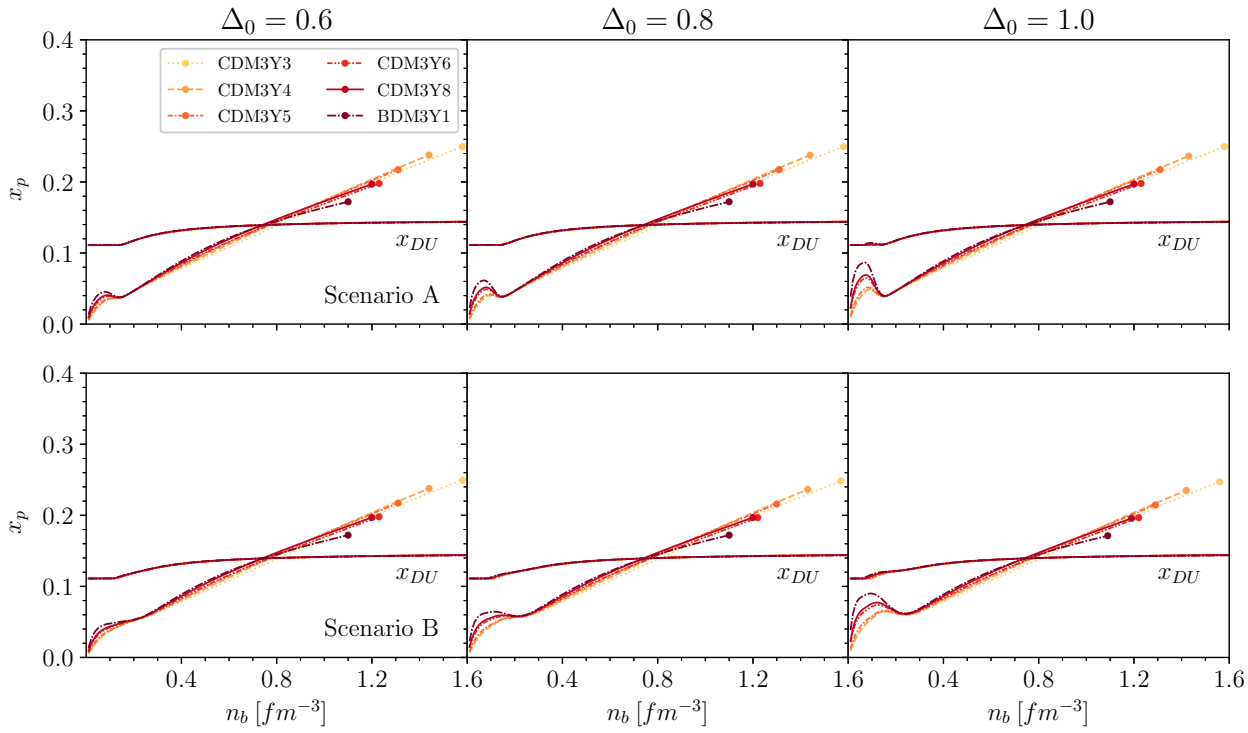

Figure 4.1: Proton fraction x_p of β-stable NM at different baryon density and spin polarization for different density-dependent NN interactions. The lower horizontal lines are the DU threshold (4.2) and the dot at the end of each line corresponds to the highest mass NS's central density of each model. The two rows of figures correspond to two previously defined scenarios, i.e. A and B.

dipole resonance by Trippa et al. (2008) or the neutron skin (Furnstahl, 2002). As shown in Figure 4.2, the symmetry energy S (2.17) of spin saturated ($\Delta = 0$) symmetric ($\delta = 0$) NM is calculated for each interaction in each scenario and compared to the empirical data. It's clear that at high baryon density n_b, the nuclear symmetry energy doesn't vary much from each others and from scenario to scenario, as well as being well within the astrophysical constraint from GW170817 by Xie and Li (2019). However, in the low density region, due to the large variation of spin polarization Δ, the calculated S only follow the empirical constraint when the NS surface is partially polarized, i.e. the total polarization case $\Delta_0 \approx 1$ is very unlikely to occur.

The same conclusion can be drawn from the energy per baryon E/A of symmetric NM (Figure 4.3), as it is in good agreement with the empirical data (Akmal et al., 1998; Gandolfi et al., 2010) at the spin saturated central region with $n_b \gtrsim 2n_0$ and even at low density if the surface is not endowed in strong magnetic field ($\Delta \approx 0$), similar to the work of Tan et al. (2021). The astrophysical constraint from GW170817, on the other hand, is much narrower than that for the nuclear symmetry energy and. Thus for this quantity, the version CDM3Y3 can be ruled out due to it being outside of the 90% region of the GW170817 constraint while the other versions with higher incompressibility K still remain within. The incompressibility

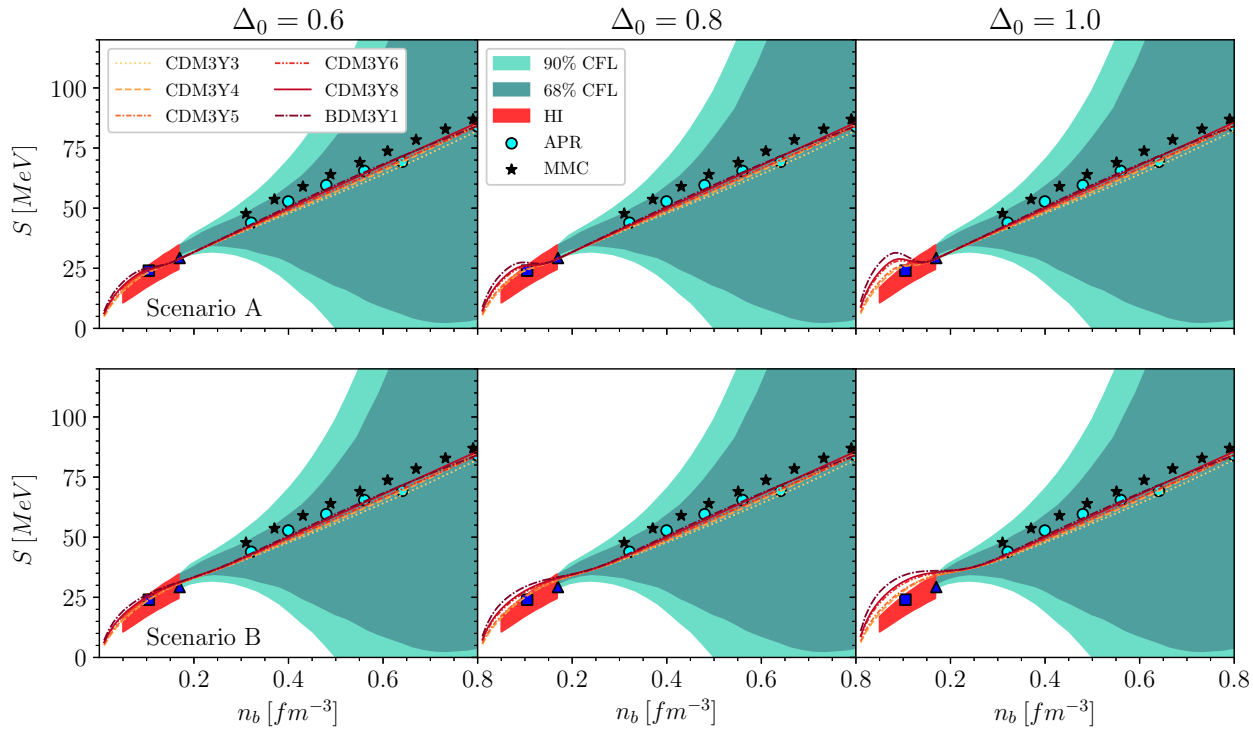

Figure 4.2: Symmetric energy S of symmetric NM at increasing polarization with 5 CDM3Yn interaction models. The shaded areas are the empirical ranges obtained from the Bayesian study (Xie and Li, 2019) of the NS of radius $R_{1.4}$ at 68% and 90% confident level (CFL) with the GW170817 event (Abbott et al., 2018). The square and triangle are the values suggested by the structure study of Trippa et al. (2008) and Furnstahl (2002). The circles and stars are the ab-initio result of Akmal et al. (1998) (APR) and microscopic Monte Carlo (MMC) calculation by Gandolfi et al. (2010).

K at saturation density n_0 is shown in the Table 4.1 for different scenario mentioned.

The incompressibility K of symmetric NM has been intensively studied in several structure studies of monopole excitations (e.g. Garg and Colo (2018)), HI collisions and refractive NN scattering (Khoa et al., 2007). The HF result in Table 4.1 gives a wide range of $K \approx 300 - 491\,MeV$ for scenario B, which is thus ruled out due to it being outside of the constrained value $K \approx 240^{+20}_{-20}\,MeV$, while scenario A returns a much smaller range of $K \approx 217 - 271\,MeV$ and agrees well with the constraint. In this scenario, the spin polarization Δ at saturation density n_0 is relatively close to 0, thus makes the result close to that of Tan et al. (2020). Apart from the nuclear incompressibility K, the present HF calculation gives rise to other quantities, i.e. the symmetry coefficient J, the slope parameter L and the curvature parameter K_{sym} (2.18), whose results are also given in Table 4.1. Recently, the values of J, L, K_{sym} are much more well determined from the study of Essick et al. (2021) by combining astrophysical data with PREX-II and chiral effective field theory, which yields $J \approx 34^{+3}_{-3}\,MeV$, $L \approx 58^{+19}_{-19}\,MeV$ and $K_{sym} \approx -107^{+128}_{-138}\,MeV$. The value of J and L obtained with HF formalism remain well within the interval suggested by the study of Essick et al. (2021), as well as the curvature K_{sym},

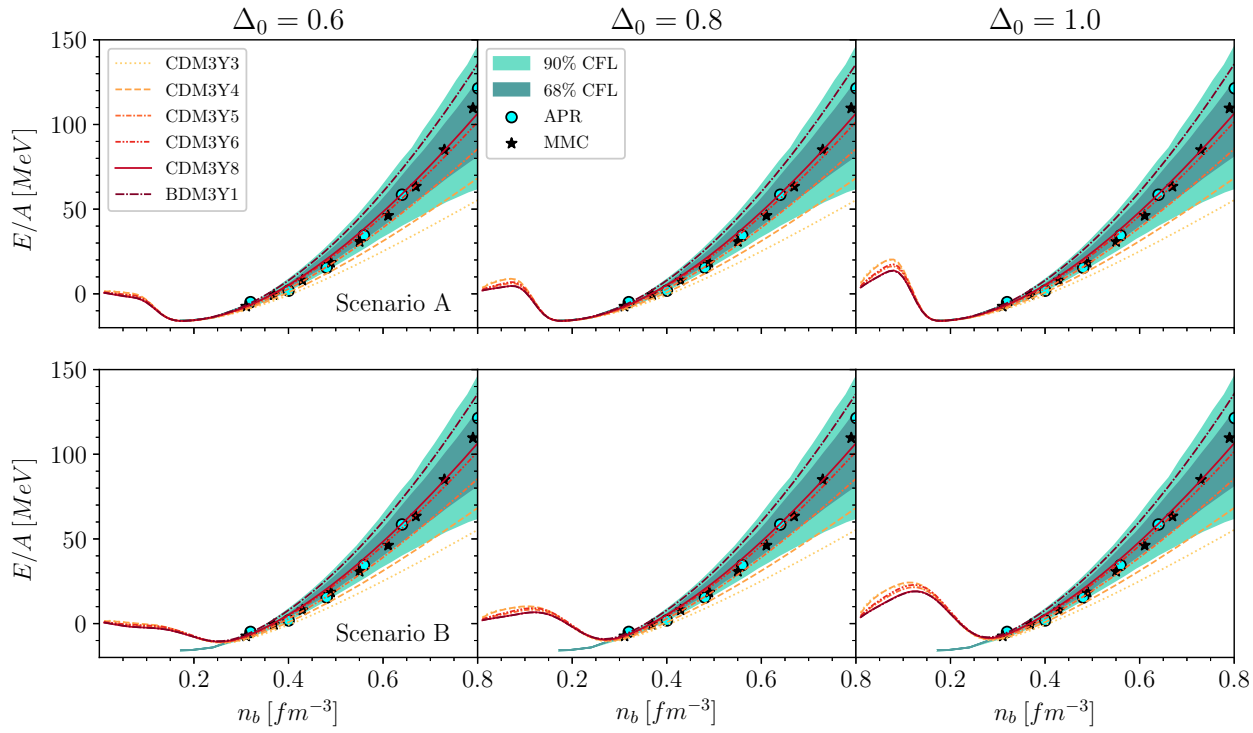

Figure 4.3: Same as Figure 4.2 for the energy per baryon E/A of symmetric NM.

however, the value of K_{sym} has not been as well determined as the other quantities, therefore it still widely ranges for different scenarios.

In Figure 4.4, we show the total pressure of NS matter $P(n_b)$ following the HF calculation of 6 different versions of the density-dependent NN interaction endowed with different scenarios. Unsurprisingly, at low density, the pressure is higher than its supposed value because of the existence of strong magnetic field at the surface. These results are simultaneously compared with the empirical pressure obtained from the "spectral" EoS inferred from the Bayesian analysis of the GW170817 event. It is clear that the larger K an interaction version has (Table 2.1), the more the generated NM can be compressed to higher pressure at high density, and the model CDM3Y3 and CDM3Y4 can be excluded since they would most likely not satisfy the constraint derived by Abbott et al. (2018), while the other 4 versions still lie inside of the 90% CFL region. In general, the pressures calculated by these 4 models follow well the empirical values from $\approx \rho_0$ to their corresponding maximum central density, i.e. the total pressure at twice and six times nuclear saturation density is within the range $P(2\rho_0) \approx 3.5^{+2.7}_{-1.7} \times 10^{34}$ and $P(6\rho_0) \approx 9.0^{+7.9}_{-2.6} \times 10^{35}\, dyn/cm^2$ at 90% CFL. Plus, at increasing spin polarization, the pressure tends to be stronger, indicated by a raise of $P(\rho_b)$ at the low density region. Taking all of the EoS constraint up until now into account, the value suggested by the empirical study tends to favor models with higher K value and smaller spin polarization.

With the previously defined NN interactions, each model generates a β-stable $npe\mu$ matter that traces a $M(R)$ relation of the NS for every different $\Delta(n_b)$ configuration, which are shown

Table 4.1: The symmetry coefficient J, slope parameter L, curvature K_{sym} of the symmetric energy (2.18) and incompressibility K (2.19) of symmetric NM, calculated using 6 different NN interactions.

Interaction	Scenario	Δ_0	J	L	K_{sym}	K
CDM3Y3	A	0.6	28.96	48.40	−68.59	217.80
		0.8	28.97	48.42	−68.54	218.295
		1.0	28.99	48.46	−68.47	218.93
	B	0.6	30.90	52.94	−62.81	300.90
		0.8	32.46	56.09	−62.46	366.29
		1.0	34.56	59.83	−66.58	450.94
CDM3Y4	A	0.6	28.98	48.40	−60.43	228.44
		0.8	28.99	48.44	−60.37	228.81
		1.0	29.00	48.47	−60.31	229.29
	B	0.6	30.73	52.43	−54.70	291.17
		0.8	32.16	55.27	−53.59	340.53
		1.0	34.09	58.72	−55.90	404.45
CDM3Y5	A	0.6	28.94	48.39	−49.55	241.78
		0.8	28.95	48.41	−49.50	242.20
		1.0	28.96	48.43	−49.44	242.74
	B	0.6	30.68	51.27	−43.81	312.46
		0.8	32.11	53.29	−41.68	368.07
		1.0	34.04	55.73	−41.68	440.09
CDM3Y6	A	0.6	28.96	48.38	−42.02	252.34
		0.8	28.97	48.39	−41.97	252.72
		1.0	28.99	48.40	−41.90	253.20
	B	0.6	31.08	49.86	−34.22	316.04
		0.8	32.77	50.67	−29.57	366.17
		1.0	35.03	51.41	−25.62	431.11
CDM3Y8	A	0.6	28.97	48.40	−28.59	257.74
		0.8	28.98	48.41	−28.55	258.21
		1.0	29.00	48.42	−28.49	258.82
	B	0.6	31.22	49.54	−22.16	337.89
		0.8	33.01	50.04	−18.40	400.98
		1.0	35.40	50.35	−15.43	482.68
BDM3Y1	A	0.6	28.99	48.38	−11.90	270.74
		0.8	29.01	48.38	−11.87	271.21
		1.0	29.03	48.37	−11.83	271.80
	B	0.6	31.47	47.03	−5.40	349.49
		0.8	33.43	45.63	0.72	411.48
		1.0	36.01	43.47	8.88	491.78

in Figure 4.5 in comparison with the GW170817 constraint (Abbott et al., 2018), as well as

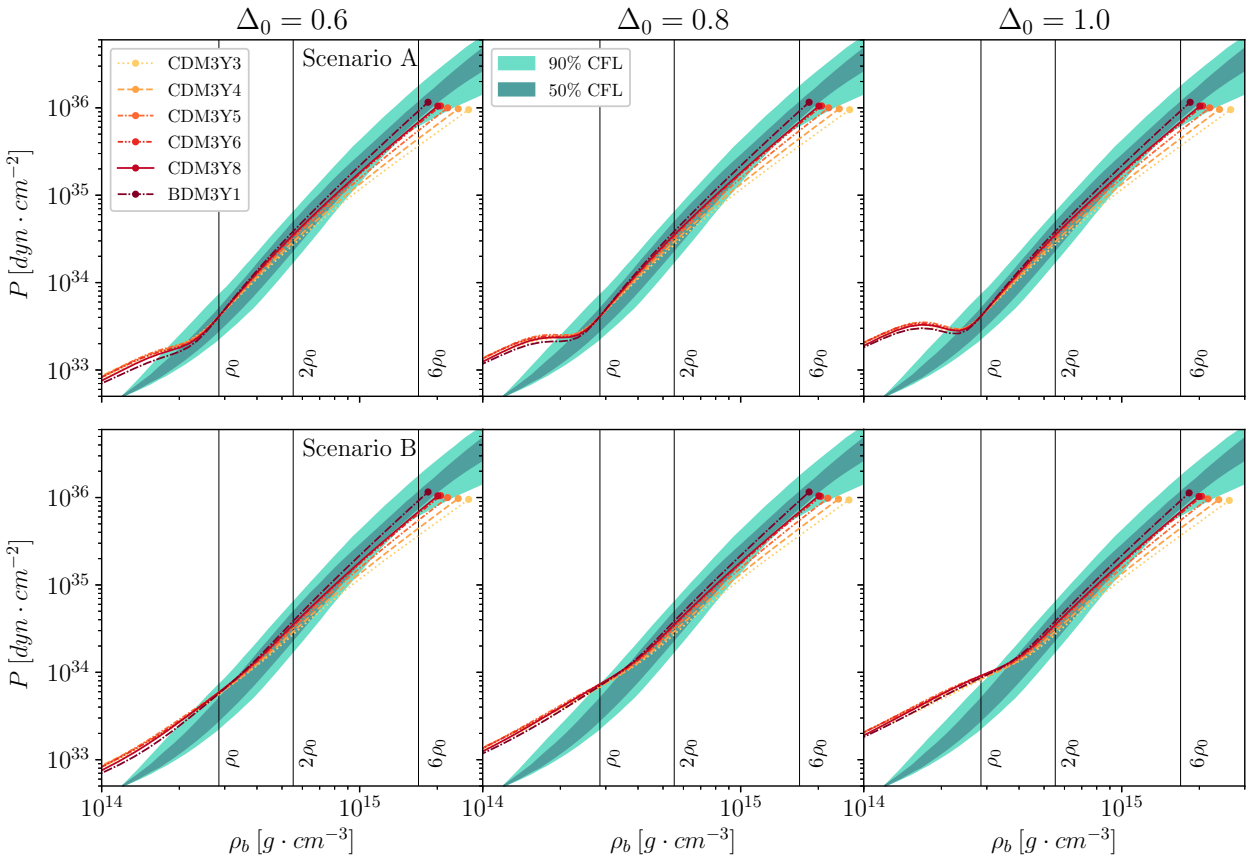

Figure 4.4: Same as Figure 4.2 for the pressure P as a function of *rest baryon mass density* ρ_b along with empirical pressure given by the "Spectral" EoS from the Bayesian analysis of the GW170817 data (Abbott et al., 2018) with 50% (light gray) and 90% (dark gray) confidence level. The dot at the end of each line corresponds to the central baryon density n_b of maximum NS mass.

the lower mass limit of the second PSR J0348+0432 ($M \approx 2.01^{+0.04}_{-0.04} M_\odot$) and the millisecond PSR J0740+6620 ($M \approx 2.14^{+0.20}_{-0.18} M_\odot$), i.e. the heaviest NSs observed so far. Notably, it is interesting that all 6 versions of the interaction here remain inside the empirical range at $M = 1.4 M_\odot$ at $\Delta_0 = 0.6$ and the scenario A when $\Delta_0 = 0.8$; the configurations with $\Delta_0 = 1.0$, unsurprisingly, give unsatisfying result, similar to the conclusion reached by Tan et al. (2020) and Tews and Schwenk (2020). The radius of a $1.4 M_\odot$ NS at $\Delta_0 = 0.6$ in the surface of the NS is $\approx 11.2 - 12.7\, km$ with scenario A, which is in agreement with the empirical value $R_{1.4} \approx 11.75^{+0.86}_{-0.81} M_\odot$ deduced from the joint analysis of two GW events GW170817 and GW190425 from two different NS mergers (Dietrich et al., 2020), and the more polarized the NS matter, the larger the NS generated is, similar to the result of Tan et al. (2020). Apart from the radius, the maximum mass of the NS corresponding to each EoS has no significant change from scenario to scenario and from the occurence of magnetic field in the NS surface (Tan et al., 2021). Beside, the observation of two heaviest pulsars PSR J0348+0432 and PSR J0740+6620 gives us more

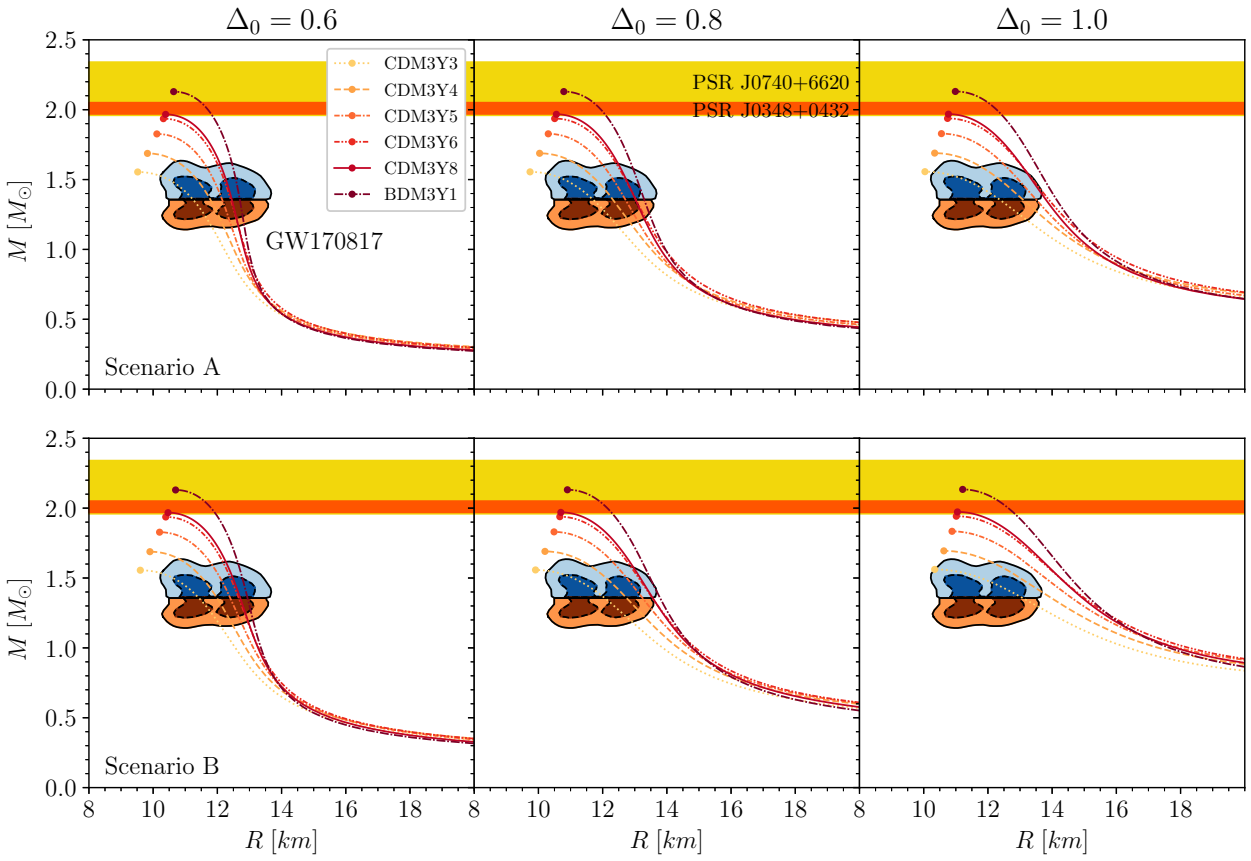

Figure 4.5: The relation between gravitational mass M and the radius R of the NS according to the corresponding model and polarization. The GW170817 constraint for NS with mass $1.4M_\odot$ is shown by the colored contour, where the blue (red) shaded area represents the heavier (lighter) NS (Abbott et al., 2018). The dot in each line indicates the maximum NS mass of the each model. The dark and light orange region indicates the mass of the second PSR J0348+0432 (Antoniadis et al., 2013) and millisecond PSR J0740+6620 (Cromartie et al., 2020) respectively.

information to further investigate the the EoS's sensitivity to the value of K and $\Delta(n_b)$; in particular, among the 6 interaction versions that satisfy the GW170817 constraint (the case of $\Delta_0 = 0.6$), only the CDM3Y6, CDM3Y8 and BDM3Y1 interactions can come close to the lower limit of these two pulsars' mass.

Alongside with the radii and gravitational mass, the tidal properties of NS can also be studied as discussed in Section 3.2. The results for GE tidal Love number's dependence on NS's gravitational mass arose from 6 versions of the EoS are shown in Figure 4.6. Similar to Perot and Chamel (2021), in this result, it is clear that the higher the order l, the less impactful the Love number k_l is for the tidal properties of the NS, i.e. k_l tends to be smaller by an order of magnitude than k_{l-1}, as expected from the multipole expansion. The 2^{nd} order is consequently dominant compared to the others. Between two scenarios A and B, at partial polarization of $\Delta_0 = 0.6$, the difference in k_l of the same order is insignificant, except for the small difference

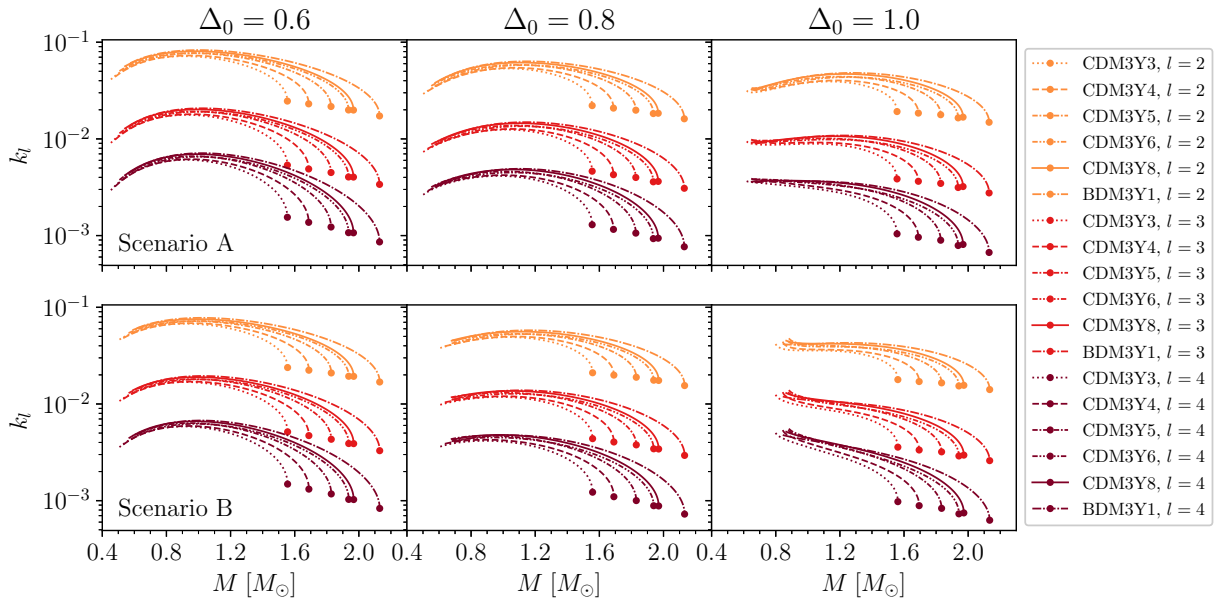

Figure 4.6: GE tidal Love number at l^{th} order k_l as function of NS mass computed with 6 density-dependent NN interaction versions at different spin polarizations. The dot at the end of each line represents the maximum gravitational mass M of the NS generated by the corresponding EoS.

in the low mass section. On the other hand, for the case of higher spin polarity in the NS surface, the results are much more distinguishable, as the computation with scenario B gives rise to a "steeper" curve of k_l. Furthermore, in general, the maximum values of k_l are at the common gravitational mass M at all orders computed so far, and this value of M seems to only depends on the value of Δ_0, where the position of maximum k_l tends to be shifted to a higher M as Δ_0 increases. Among these tidal parameters, the only one that has been constrained by far is the dominant 2^{nd} order Love number, which is investigated through the closely related dimensionless tidal deformability parameter of second order Λ_2 (3.10) and whose results are given in Figure 4.7. In the study of Abbott et al. (2018), the value of Λ_2 is accepted to be $\Lambda_2 \approx 190^{+390}_{-120}$ at $M = 1.4M_\odot$. It is interesting to note that for all cases in this study, this constraint tolerates all EoSs and scenarios, as well as the value of Δ_0, thus no further exclusion can be done with this parameter. It's worth mentioning that the nuclear incompressibility K plays a significant role in determining the tidal deformability Λ_2 as when K varies from version to version (CDM3Y3 to BDM3Y1), the value of Λ_2 increases by ≈ 3 times for the scenario A of $\Delta_0 = 0.6$ case, the same can be said for the different configuration of $\Delta(n_b)$. Testing the values of k_l at higher orders can also be done by evaluating the tidal correction of the GW waveform from inspiralling NSs within the PN theory, i.e. the GE contribution of order $(2l+1)$PN to the phase of GW signal is (Perot and Chamel, 2021; Yagi, 2014)

$$\Psi_l = -\sum_{i=1}^{2}\left[\frac{5}{16}\frac{(2l-1)!!(4l+3)(l+1)}{(4l-3)(2l-3)}\Lambda_{l,i}X_i^{2l-1}x^{2l-3/2} + \frac{9}{16}\delta_{l2}\Lambda_{2,i}\frac{X_i^4}{\eta}x^{5/2}\right] + \mathcal{O}(x^{2l-1/2}) \quad (4.3)$$

where $i = 1, 2$ is the index distinguishing the two NSs of the system, $x = (G\pi Mf/c^3)^{2/3}$, f is the GW signal frequency, $M = M_1 + M_2$, $X_i = M_i/M$ and $\eta = M_1M_2/M^2$.

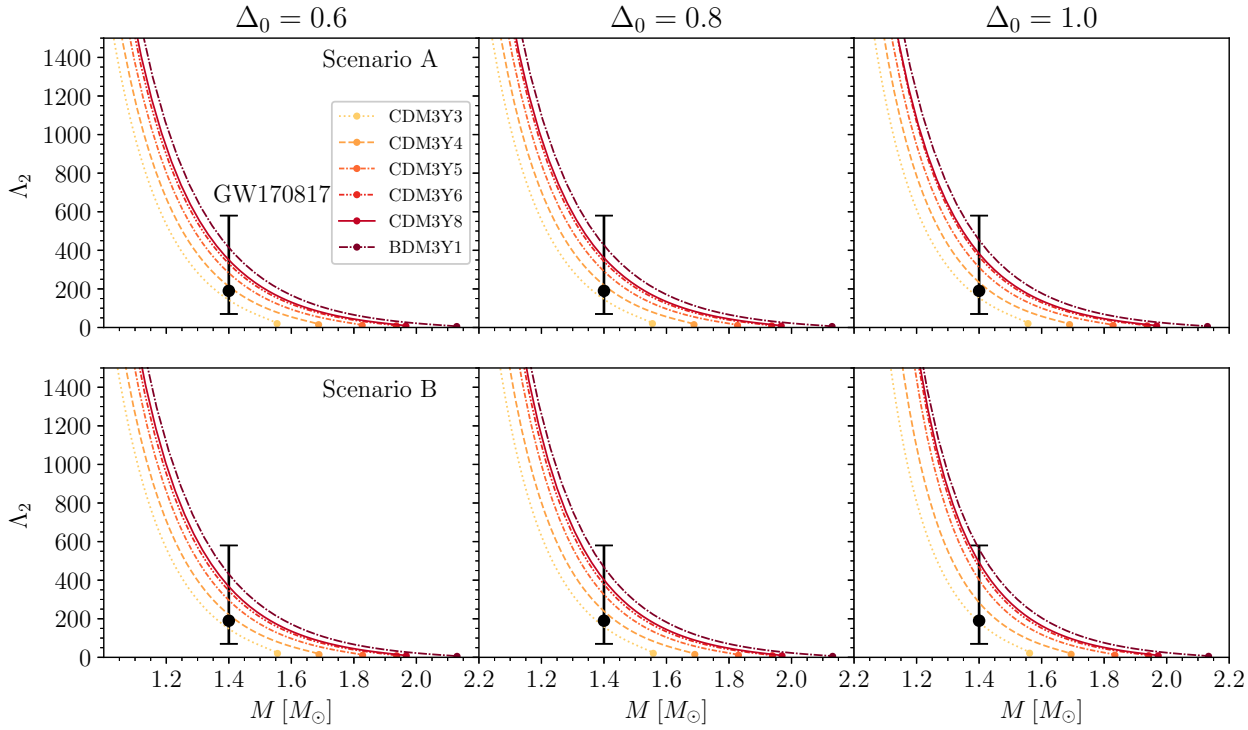

Figure 4.7: Dimensionless GE tidal deformability parameter of 2nd order Λ_2 of different CDM3Yn models with varying Δ. The vertical bar is the empirical tidal deformability constraint $\Lambda_2 \approx 190^{+390}_{-120}$ at $1.4M_\odot$, obtained from the Bayesian analysis of GW170817 data with 90% confidence level (Abbott et al., 2018).

The gravito-magnetic tidal Love numbers j_l contribute more weakly to the GW phase compared to that of their GE counterpart, as the GM terms only appear from higher orders of $(2l+2)$PN, where the first correction at 6PN is given by (Perot and Chamel, 2021; Yagi, 2017)

$$\tilde{\Psi}_2 = \sum_{i=1}^{2} \frac{5}{224}\sigma_{2,i}\frac{X_i^4}{\eta}\left(X_i - 1037X_j\right)x^{7/2} + \mathcal{O}(x^{9/2}) \tag{4.4}$$

The GM tidal Love numbers of second, third and fourth order computed with 6 different EoSs are shown in Figure 4.8 for strictly static fluid and 4.9 for irrotational fluid as discussed in Section 3.2. Apart from the same trends as the GE tidal Love numbers discussed previously, the GM Love numbers' values do not have much variation as Δ_0 increases in each scenario, as the shape of each curves in Figure 4.8 doesn't differ far from each others except for the difference in range of gravitational mass M. The value of j_l corresponding to the GM pertubation of irrotational fluid (Figure 4.9), on the other hand, stands out from the other two types of Love numbers, where its value is completely negative, albeit having the same magnitude as that of static fluid, this type of fluid motion is stated to be more realistic in this case due to it being

driven by the tides (Perot and Chamel, 2021; Pani et al., 2018). In this case, the lines traced by each interation appear to reach maximum value at the maximum M at the leading terms only, rather than having a local maxima in between. The dominance of the 2$^{\text{nd}}$ order terms are clear in all cases, where the difference of around one order of magnitude is remained. Notably, for the GM terms corresponding with each NN interaction, at higher order l, the NS mass at maximum j_l seems to become smaller. One more interesting result is that the magnitudes of j_l for two types of fluid are also comparable but is smaller than their GE counterpart by one order of magnitude, similar to the conclusion reached by Perot and Chamel (2021).

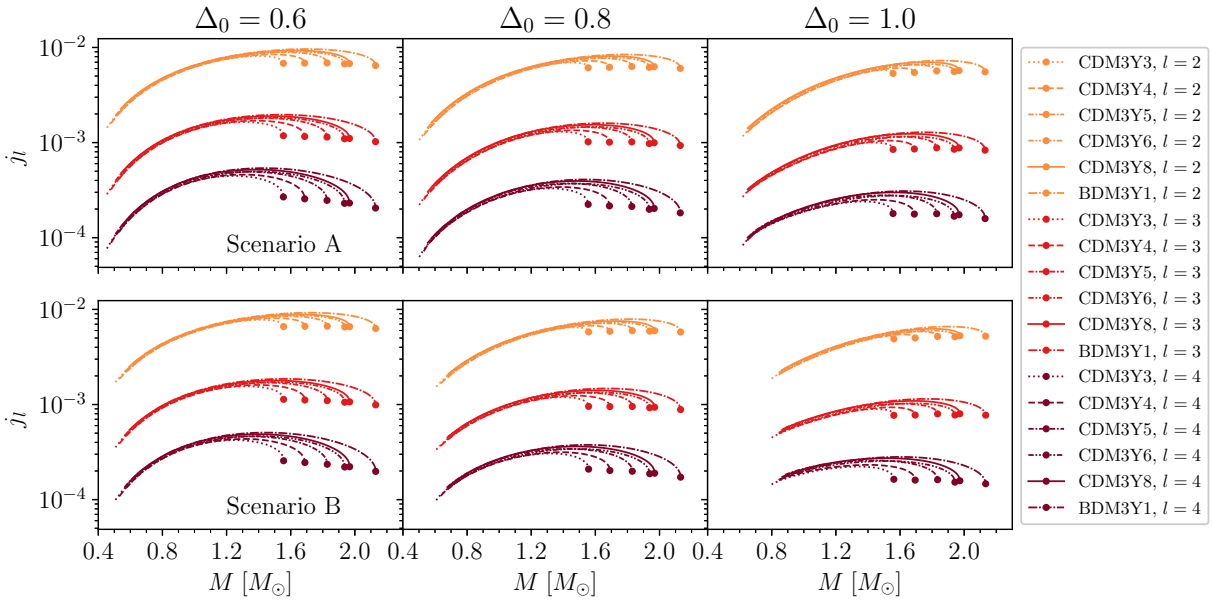

Figure 4.8: GM tidal Love number at l^{nd} order j_l as function of NS mass computed with CDM3Yn models of *strictly static fluid* at different polarizations.

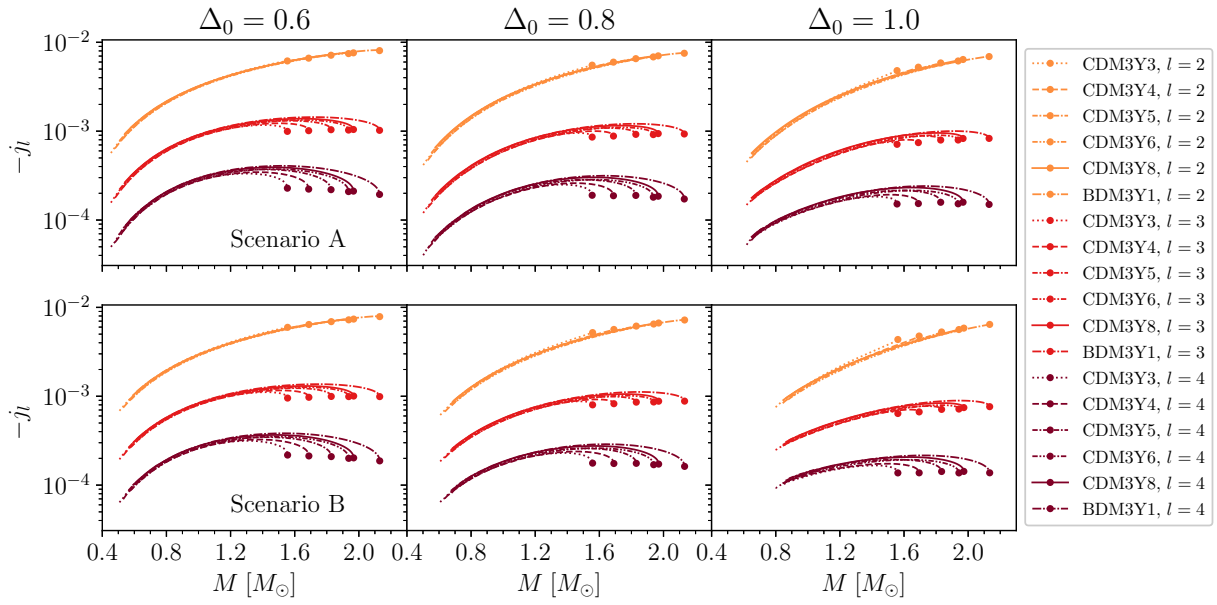

Figure 4.9: GM tidal Love number at l^{nd} order j_l as function of NS mass computed with CDM3Yn models of *irrotational fluid* at different polarizations.

Chapter 5

Conclusions

By extending the 6 current versions of density-dependent NN interaction (Tan et al., 2021), we have been able to include the description of spin polarization effect of NS matter under strong magnetic field over a wider range of K into the EoS of NM using the nonrelativistic HF formalism. The density-dependence of the polarization Δ was also taken into account as different situations regarding the localization of magnetic field at the surface of NS, adopting from the study of Tan et al. (2020). From these scenarios and EoSs, the case of total polarization at the surface ($\Delta_0 = 1.0$) has been ruled out, as it failed most of the criteria demanded by the empirical constraints. In general, concerning the EoS of NM, the empirical ranges deduced for symmetry energy S, energy per baryon of symmetric NM E/A and total pressure P seem to favor partial polarization, or in particular, the cases with lower Δ overall. Among these 6 versions of EoS, the CDM3Y3 and CDM3Y4 interactions are very unlikely to occur in reality, as the EoS generated by these interactions are usually outside of the 90% CFL boundary obtained from astrophysical observation and analysis at high density.

The macroscopic properties of the NS, on the other hand, only the scenarios with $\Delta_0 = 0.6$ and the case of $\Delta_0 = 0.8$ at the scenario A succeed in staying within the GW170817 constraint (Abbott et al., 2018), which supports the suggestion of the blue kilonova ejecta of GW170817 coming from a magnetar (Metzger et al., 2018; Tan et al., 2020). Furthermore, only the CDM3Y6, CDM3Y8 and BDM3Y1 in these scenarios can come close to satisfy the lower mass limit of the two heaviest pulsars ever observed, i.e. PSR J0348+0432 and PSR J0740+6620. The tidal deformability parameter Λ_2, surprisingly, do not provide further constraint, as all cases are within the accepted range obtained by Abbott et al. (2018). Beside, higher orders of multipoles up to the 4^{th} order have been investigated for both gravito-electric and gravito-magnetic tidal perturbations. The common diminishing effects as the order l increases are founded for all cases, as well as the dominance of the GE tidal Love numbers in magnitude compared to the GM ones, which is understandable with the contribution of each term in the phase of GW signal (Abdelsalhin et al., 2018). The observation of GM tidal deformability can be very possibly used as an additional test of Einstein's theory of GR, since these effects are not presented in Newtonian physics. More information on the EoS of NS matter can also be further constrained with the potential observation of the higher order terms, which might be possible with the third-generation GW detectors.

Bibliography

Abbott, B., Abbott, R., Abbott, T., Abraham, S., Acernese, F., Ackley, K., Adams, C., Adhikari, R., Adya, V., Affeldt, C., et al. (2020). GW190425: observation of a compact binary coalescence with total mass $\sim 3.4 M_{\odot}$. *The Astrophysical Journal Letters*, 892(1):L3.

Abbott, B. P., Abbott, R., Abbott, T., Acernese, F., Ackley, K., Adams, C., Adams, T., Addesso, P., Adhikari, R., Adya, V., et al. (2017). GW170817: observation of gravitational waves from a binary neutron star inspiral. *Physical Review Letters*, 119(16):161101.

Abbott, B. P., Abbott, R., Abbott, T., Acernese, F., Ackley, K., Adams, C., Adams, T., Addesso, P., Adhikari, R. X., Adya, V. B., et al. (2018). GW170817: Measurements of neutron star radii and equation of state. *Physical review letters*, 121(16):161101.

Abdelsalhin, T., Gualtieri, L., and Pani, P. (2018). Post-Newtonian spin-tidal couplings for compact binaries. *Physical Review D*, 98(10):104046.

Akmal, A., Pandharipande, V., and Ravenhall, D. a. (1998). Equation of state of nucleon matter and neutron star structure. *Physical Review C*, 58(3):1804.

Anantaraman, N., Toki, H., and Bertsch, G. (1983). An effective interaction for inelastic scattering derived from the Paris potential. *Nuclear Physics A*, 398(2):269–278.

Antoniadis, J., Freire, P. C., Wex, N., Tauris, T. M., Lynch, R. S., van Kerkwijk, M. H., Kramer, M., Bassa, C., Dhillon, V. S., Driebe, T., et al. (2013). A massive pulsar in a compact relativistic binary. *Science*, 340(6131).

Baym, G. and Pethick, C. (1975). Neutron stars. *Annual Review of Nuclear Science*, 25(1):27–77.

Cromartie, H. T., Fonseca, E., Ransom, S. M., Demorest, P. B., Arzoumanian, Z., Blumer, H., Brook, P. R., DeCesar, M. E., Dolch, T., Ellis, J. A., et al. (2020). Relativistic Shapiro delay measurements of an extremely massive millisecond pulsar. *Nature Astronomy*, 4(1):72–76.

Damour, T. and Nagar, A. (2009). Relativistic tidal properties of neutron stars. *Physical Review D*, 80(8):084035.

Dietrich, T., Coughlin, M. W., Pang, P. T., Bulla, M., Heinzel, J., Issa, L., Tews, I., and Antier, S. (2020). Multimessenger constraints on the neutron-star equation of state and the Hubble constant. *Science*, 370(6523):1450–1453.

Douchin, F. and Haensel, P. (2001). A unified equation of state of dense matter and neutron star structure. *Astronomy & Astrophysics*, 380(1):151–167.

Douchin, F., Haensel, P., and Meyer, J. (2000). Nuclear surface and curvature properties for SLy Skyrme forces and nuclei in the inner neutron-star crust. *Nuclear Physics A*, 665(3-4):419–446.

Essick, R., Tews, I., Landry, P., and Schwenk, A. (2021). Astrophysical Constraints on the Symmetry Energy and the Neutron Skin of ^{208}Pb with Minimal Modeling Assumptions. *arXiv preprint arXiv:2102.10074*.

Evans, P., Cenko, S., Kennea, J., Emery, S., Kuin, N., Korobkin, O., Wollaeger, R., Fryer, C., Madsen, K., Harrison, F., et al. (2017). Swift and NuSTAR observations of GW170817: detection of a blue kilonova. *Science*, 358(6370):1565–1570.

Fujisawa, K. and Kisaka, S. (2014). Magnetic field configurations of a magnetar throughout its interior and exterior–core, crust and magnetosphere. *Monthly Notices of the Royal Astronomical Society*, 445(3):2777–2793.

Furnstahl, R. (2002). Neutron radii in mean-field models. *Nuclear Physics A*, 706(1-2):85–110.

Gandolfi, S., Illarionov, A. Y., Fantoni, S., Miller, J., Pederiva, F., and Schmidt, K. (2010). Microscopic calculation of the equation of state of nuclear matter and neutron star structure. *Monthly Notices of the Royal Astronomical Society: Letters*, 404(1):L35–L39.

Garg, U. and Colo, G. (2018). The compression-mode giant resonances and nuclear incompressibility. *Progress in Particle and Nuclear Physics*, 101:55–95.

Glendenning, N. K. (2012). *Compact stars: Nuclear physics, particle physics and general relativity*. Springer Science & Business Media.

Greiner, W. and Maruhn, J. A. (1996). *Nuclear models*. Springer.

Hinderer, T. (2008). Tidal Love numbers of neutron stars. *The Astrophysical Journal*, 677(2):1216.

Hinderer, T., Lackey, B. D., Lang, R. N., and Read, J. S. (2010). Tidal deformability of neutron stars with realistic equations of state and their gravitational wave signatures in binary inspiral. *Physical Review D*, 81(12):123016.

Horowitz, C., Brown, E., Kim, Y., Lynch, W., Michaels, R., Ono, A., Piekarewicz, J., Tsang, M., and Wolter, H. (2014). A way forward in the study of the symmetry energy: experiment, theory, and observation. *Journal of Physics G: Nuclear and Particle Physics*, 41(9):093001.

Khoa, D. T. and Satchler, G. (2000). Generalized folding model for elastic and inelastic nucleus–nucleus scattering using realistic density dependent nucleon–nucleon interaction. *Nuclear Physics A*, 668(1-4):3–41.

Khoa, D. T., Satchler, G., and Von Oertzen, W. (1997). Nuclear incompressibility and density dependent NN interactions in the folding model for nucleus-nucleus potentials. *Physical Review C*, 56(2):954.

Khoa, D. T., Von Oertzen, W., Bohlen, H., and Ohkubo, S. (2007). Nuclear rainbow scattering and nucleus–nucleus potential. *Journal of Physics G: Nuclear and Particle Physics*, 34(3):R111.

Khoa, D. T., Von Oertzen, W., and Ogloblin, A. (1996). Study of the equation of state for asymmetric nuclear matter and interaction potential between neutron-rich nuclei using the density-dependent M3Y interaction. *Nuclear Physics A*, 602(1):98–132.

Lattimer, J. M. (2014). Symmetry energy in nuclei and neutron stars. *Nuclear Physics A*, 928:276–295.

Lattimer, J. M., Pethick, C., Prakash, M., and Haensel, P. (1991). Direct URCA process in neutron stars. *Physical review letters*, 66(21):2701.

Lattimer, J. M. and Prakash, M. (2004). The physics of neutron stars. *science*, 304(5670):536–542.

Le Tiec, A. and Casals, M. (2021). Spinning black holes fall in love. *Physical Review Letters*, 126(13):131102.

Li, B.-A., Chen, L.-W., and Ko, C. M. (2008). Recent progress and new challenges in isospin physics with heavy-ion reactions. *Physics Reports*, 464(4-6):113–281.

Loan, D. T., Tan, N. H., Khoa, D. T., and Margueron, J. (2011). Equation of state of neutron star matter, and the nuclear symmetry energy. *Physical Review C*, 83(6):065809.

Metzger, B. D., Thompson, T. A., and Quataert, E. (2018). A magnetar origin for the kilonova ejecta in GW170817. *The Astrophysical Journal*, 856(2):101.

Moustakidis, C. C. and Panos, C. (2009). Equation of state for β-stable hot nuclear matter. *Physical Review C*, 79(4):045806.

Ono, A., Danielewicz, P., Friedman, W., Lynch, W., and Tsang, M. (2003). Isospin fractionation and isoscaling in dynamical simulations of nuclear collisions. *Physical Review C*, 68(5):051601.

Pani, P., Gualtieri, L., Abdelsalhin, T., and Jiménez-Forteza, X. (2018). Magnetic tidal Love numbers clarified. *Physical Review D*, 98(12):124023.

Perot, L. and Chamel, N. (2021). Role of dense matter in tidal deformations of inspiralling neutron stars and in gravitational waveforms with unified equations of state. *Physical Review C*, 103(2):025801.

Tan, N. H., Khoa, D. T., and Loan, D. T. (2020). Spin-polarized β-stable neutron star matter: The nuclear symmetry energy and GW170817 constraint. *Physical Review C*, 102(4):045809.

Tan, N. H., Khoa, D. T., and Loan, D. T. (2021). Equation of state of asymmetric nuclear matter and the tidal deformability of neutron star. *arXiv preprint arXiv:2104.09121*.

Tan, N. H., Loan, D. T., Khoa, D. T., and Margueron, J. (2016). Mean-field study of hot β-stable protoneutron star matter: Impact of the symmetry energy and nucleon effective mass. *Physical Review C*, 93(3):035806.

Tews, I. and Schwenk, A. (2020). Spin-polarized neutron matter, the maximum mass of neutron stars, and GW170817. *The Astrophysical Journal*, 892(1):14.

Thân, H. S. (2010). *UFR SCIENTIFIQUE D'ORSAY INSTITUT DE PHYSIQUE NUCLEAIRE D'ORSAY*. PhD thesis, Citeseer.

Trippa, L., Colò, G., and Vigezzi, E. (2008). Giant dipole resonance as a quantitative constraint on the symmetry energy. *Physical Review C*, 77(6):061304.

Tsang, M., Chajecki, Z., Coupland, D., Danielewicz, P., Famiano, F., Hodges, R., Kilburn, M., Lu, F., Lynch, W., Winkelbauer, J., et al. (2011). Constraints on the density dependence of the symmetry energy from heavy-ion collisions. *Progress in Particle and Nuclear Physics*, 66(2):400–404.

Vidana, I. and Bombaci, I. (2002). Equation of state and magnetic susceptibility of spin polarized isospin asymmetric nuclear matter. *Physical Review C*, 66(4):045801.

Xie, W.-J. and Li, B.-A. (2019). Bayesian inference of high-density nuclear symmetry energy from radii of canonical neutron stars. *The Astrophysical Journal*, 883(2):174.

Yagi, K. (2014). Multipole love relations. *Physical Review D*, 89(4):043011.

Yagi, K. (2017). Erratum: Multipole love relations [phys. rev. d 89, 043011 (2014)]. *Physical Review D*, 96(12):129904.